

IMPROVING CLOUD AND MOISTURE REPRESENTATION
BY ASSIMILATING GOES SOUNDER PRODUCTS
INTO NUMERICAL WEATHER PREDICTION INITIAL CONDITIONS

by

Jordan J. Gerth

A thesis submitted in partial fulfillment of
the requirements for the degree of

Master of Science

(Atmospheric and Oceanic Sciences)

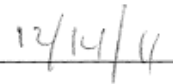
at the

UNIVERSITY OF WISCONSIN-MADISON

2011

APPROVED





Dr. Steven Ackerman

Date

Professor, Department of Atmospheric and Oceanic Sciences

Submitted for degree on 16 December 2011

Improving Cloud and Moisture Representation by Assimilating GOES Sounder Products into Numerical Weather Prediction Initial Conditions

Jordan J. Gerth¹

Department of Atmospheric and Oceanic Sciences
Cooperative Institute for Meteorological Satellite Studies
University of Wisconsin, Madison, Wisconsin

¹ *Corresponding author address:* Jordan Gerth, Cooperative Institute for Meteorological Satellite Studies, University of Wisconsin, 1225 W. Dayton St., Madison, WI 53706.
E-mail: jordang@ssec.wisc.edu

Abstract

Adequately forecasting moist processes resulting from mesoscale and synoptic weather system dynamics is an active problem in the realm of operational meteorology.

Numerical weather prediction has been a beneficial tool for studying and forecasting such processes. A number of parameterizations have been developed to facilitate the solution while suppressing numerical instabilities and controlling budgets of conserved quantities. However, the ideal model must be initialized with an analysis that adequately resolves variations in the moisture concentration and cloud cover on the same scale as the simulation grid spacing to attain the most accurate forecast. Due to a very sparse upper-air observation network across the United States, the only way to accomplish this is with satellite products.

This paper develops a methodology for an experiment with several parallel regional Weather Research and Forecasting (WRF) model simulations initialized with satellite-based retrievals. The intent is to clarify the impact of observations, in the form of retrievals, from the Geostationary Operational Environmental Satellite (GOES) Sounder on 12, 24, and 36-hour WRF model forecasts of precipitable water, low-level relative humidity, precipitation, and sky cover. Two experimental analyses are built from a CIMSS Regional Assimilation System (CRAS) pre-forecast spin-up. The CRAS assimilates precipitable water and cloud products derived from the GOES Sounder. An experimentation period between late September and early October 2011 found that the majority of impact in the experimental simulations compared to the control is recognized in the total precipitable water field over the first 12 hours. In some cases, this resulted in an improved precipitation forecast. Cloud cover results were inconclusive, though a new technique developed for use in the CRAS outperformed the current WRF cloud fraction approach.

Executive Summary

The purpose of this study was to assess the impact of Geostationary Operational Environmental Satellite (GOES) Sounder moisture retrievals in short-term predictions using the Weather Research and Forecasting model (WRF), which is commonly used on regional scales at National Weather Service (NWS) forecast offices. The Advanced Research WRF (ARW) configuration used for this investigation included the Kain-Fritsch convective scheme. This is a mass flux scheme with sensitivity to relative humidity in the middle and upper troposphere. The model domain was Lambert Conformal over the north central United States with 100 grid points in both horizontal dimensions spaced every 20 km.

In comparison, retrievals from the GOES Sounder are available approximately every 10 km at hourly intervals over the continental United States. The Cooperative Institute for Meteorological Satellite Studies (CIMSS) Regional Assimilation System (CRAS) routinely takes these retrievals and maps them to a model grid with background mass fields from the Global Forecast System (GFS). The CRAS framework, which applies a one-dimensional variational method with a strong constraint to adjust moisture content (precipitable water) for clear fields of view in three vertical layers, but not the vertical gradients within those layers, was leveraged in this study. The CRAS also adds or subtracts clouds based on GOES Sounder cloud top pressure products.

For this study, the WRF model was initialized from CRAS input in both of the experimental runs. The control run, the WRFX, contained initial and boundary conditions from the GFS. The GFS does not assimilate GOES Sounder observations over land as of this writing. The WRFY experiment run obtained boundary conditions from the CRAS, while the WRFZ experiment run obtained boundary conditions from the GFS. The WRFY also used an analysis formed from a 12-hour CRAS pre-forecast procedure, whereas the WRFZ analysis was the result of a single assimilation step at the initialization time using the previous GFS' six-hour forecast as the background. The duration of all WRF model simulations was 36 hours.

The experiment period ran from 00 UTC 28 September 2011 to 00 UTC 8 October 2011. Other cases in October and November were also considered to

demonstrate performance of the assimilation technique for high-impact weather. A small precipitable water improvement was noted for 12-hour forecasts using the WRFZ over the WRFX. This result was substantiated by the use of Global Positioning System (GPS) integrated precipitable water point measurements as truth, as well as the North American Mesoscale (NAM) model analyses, which contain GPS precipitable water measurements, but primarily in-situ moisture observations as input. The changes to the precipitable water analysis as a result of the assimilation procedure also altered surface precipitation forecasts, as shown in an example case. Most of the moisture improvement by assimilation was found to be confined to the middle and upper troposphere, where the weighting functions for water vapor emission wavelengths sensed by the GOES Sounder typically peak during the summer months. Observation skill in the boundary layer, closer to the surface, is typically only possible in drier regimes common of winter months.

Performance of the WRF and CRAS models for short-term cloud fraction predictions was also evaluated. For total sky cover, the WRF model control and experiment runs collectively underperformed compared to the CRAS. A special cloud fraction algorithm, using a celestial dome technique coupled with a cloud-to-precipitation auto-conversion limit ratio, was developed for the CRAS to better match the NWS National Digital Forecast Database (NDFD) forecasts. Since the default WRF model cloud fraction algorithm takes an average of three tropospheric layers, which is not the conventional understanding of cloud cover, a technique was implemented to find the maximum fraction of the three layers for comparison with the CRAS and default WRF algorithms. The maximum fraction approach did perform better than the default, but not as well as the CRAS. However, even using the maximum fraction approach, differences in error between the control and experimental WRF runs were unable to be explained as a consequence of the assimilation process.

In lieu of these findings, it was evident that future work must focus on the development and clarification of cloud fraction for uses in numerical weather prediction and conventional forecasts. Furthermore, our geostationary observing platform places a constraint on our ability to monitor and forecast weather patterns because it is unable to assess vertical moisture and temperature gradients without substantial reliance on a

background from radiosondes or in-situ measurements. The results presented here confirm this. It follows from a basic tenet of numerical weather prediction that remotely-sensed observations at the same spatial and temporal scale as weather prediction models would usually lead to increased performance of those models. Without enhancements to increase the number of observations, improve vertical spectral resolution, and decrease the error, numerical weather prediction skill will eventually plateau.

Acknowledgements

Dr. Steven Ackerman, a professor of atmospheric and oceanic sciences at the University at Wisconsin, and Robert Aune, a research meteorologist with the National Oceanic and Atmospheric Administration (NOAA), provided guidance and assistance in the execution of this study. The worth of their advice and interest in a thorough scientific process is immeasurable. The University of Wisconsin's Space Science and Engineering Center (SSEC) was a valuable location to perform this study due to its academic wealth, integral science staff, and superior computing resources.

I would like to thank the Wisconsin Space Grant Consortium (WSGC), the National Aeronautics and Space Administration (NASA), NOAA, specifically the National Environmental Satellite, Data, and Information Service (NESDIS), the Geostationary Operational Environmental Satellite R-Series (GOES-R) Program Office and the National Weather Service (NWS), and SSEC for the ability and support to conduct this research, as well as the researchers at the Cooperative Institute for Meteorological Satellite Studies (CIMSS) for their unending support in guiding my academic and professional pursuits.

Lastly, the faculty in the Department of Atmospheric and Oceanic Sciences at the University of Wisconsin deserves recognition for building a world-class program for undergraduate and graduate meteorological studies. Specifically, thanks are extended to Dr. Gregory Tripoli and Dr. Jonathan Martin for their review of this thesis.

Table of Contents

1.	Introduction.....	1
2.	Background of problem	4
a.	Precipitation efficiency	6
b.	Conservation of enthalpy	7
c.	Advanced Research WRF configuration	8
Flux Renormalization.....	10	
Convective Scheme.....	11	
3.	Data and methodology	11
a.	Configuration of control and experimental WRF runs	12
b.	Building analysis from GOES Sounder retrievals with CRAS.....	14
c.	Summary of methodology behind GOES Sounder moisture retrievals	16
d.	Incorporation of the clear retrieval into the model-simulated atmosphere	16
e.	History of the approach.....	17
f.	Assimilation procedure	18
g.	Critique on likelihood of success	20
h.	Adjustments due to cloudy fields of view.....	21
i.	Experiment domain and justification	22
j.	Initial evaluations.....	22
4.	Precipitable water results	24
a.	Error of NCEP operational model analyses compared to GPS-IPW	26
b.	Error of experiment and control WRF analyses compared to GPS-IPW.....	27
c.	Error of experiment and control WRF analyses compared to GOES-13 retrievals.....	27
d.	Error of NCEP operational model analyses compared to GOES-13 retrievals	29
e.	Case study	30
f.	Error of experiment and control WRF 12-hour forecasts compared to GPS-IPW	31
g.	Error of experiment and control WRF 12-hour forecasts compared to NAM analysis.....	32
h.	Error of relative humidity forecasts compared to NAM analysis	33
i.	Impact on precipitation	35
5.	Cloud fraction results	36
a.	WRF cloud fraction methodology	37
b.	Motivation for CRAS cloud fraction	39
c.	CRAS cloud fraction methodology.....	40
d.	Results.....	42
6.	Conclusions.....	45
	References.....	48
	Tables.....	54
	Figures.....	61

List of Tables

TABLE 1. The core configuration for the WRF model used in the experiment.	54
TABLE 2. Mean values of MAE and RMSE for NCEP model analyses of total precipitable water compared to GPS-IPW over the period from 00 UTC 28 September 2011 to 00 UTC 8 October 2011.	55
TABLE 3. Mean values of MAE and RMSE for WRF model analyses of total precipitable water compared to GPS-IPW over the period from 00 UTC 28 September 2011 to 00 UTC 8 October 2011.	55
TABLE 4. Mean values of MAE and RMSE for WRF model analyses of total precipitable water compared to GOES-13 Sounder Ma retrievals over the period from 00 UTC 28 September 2011 to 00 UTC 8 October 2011.....	56
TABLE 5. Mean values of MAE and RMSE for NCEP model analyses of total precipitable water compared to GOES-13 Sounder Ma retrievals over the period from 00 UTC 28 September 2011 to 00 UTC 8 October 2011.....	56
TABLE 6. Mean values of MAE and RMSE for WRF model 12-hour forecasts of total precipitable water compared to GPS-IPW over the period from 00 UTC 28 September 2011 to 00 UTC 8 October 2011.	57
TABLE 7. Mean values of MAE and RMSE for WRF model 12-hour forecasts of total precipitable water compared to NAM analyses over the period from 00 UTC 28 September 2011 to 00 UTC 8 October 2011.	57
TABLE 8. Mean values of MAE and RMSE for WRF model 24-hour forecasts of total precipitable water compared to NAM analyses over the period from 00 UTC 28 September 2011 to 00 UTC 8 October 2011.	58
TABLE 9. Mean values of MAE and RMSE for WRF model 36-hour forecasts of total precipitable water compared to NAM analyses over the period from 00 UTC 28 September 2011 to 00 UTC 8 October 2011.	58
TABLE 10. Mean values of MAE of relative humidity at 700 hPa and 850 hPa compared to NAM analyses over the period from 00 UTC 28 September 2011 to 00 UTC 8 October 2011.....	59
TABLE 11. Mean values of MAE of total sky cover for WRF model maximum fraction 12-hour forecasts compared to NAM analyses and NDFD one-hour forecasts over the period from 00 UTC 28 September 2011 to 00 UTC 8 October 2011.....	59

TABLE 12. Mean values of MAE of total sky cover for WRF model default fraction 12-hour forecasts compared to NAM analyses and NDFD one-hour forecasts over the period from 00 UTC 28 September 2011 to 00 UTC 8 October 2011.	60
--	----

List of Figures

FIG. 1. Water vapor weighting functions for the GOES-13 Sounder and future GOES-R ABI in an idealized mid-latitude summer atmosphere sounding.	61
FIG. 2. A skew-T log-P diagram comparing the radiosonde sounding from International Falls, Minnesota, to the GFS analysis, valid at 12 UTC on 13 November 2011.	62
FIG. 3. A skew-T log-P diagram comparing the radiosonde sounding from International Falls, Minnesota, to the GFS analysis adjusted with a water vapor retrieval, valid at 12 UTC on 13 November 2011.	63
FIG. 4. The 36-hour accumulated precipitation ending 12 UTC 1 September 2010 from various WRF runs initialized at 00 UTC 31 August 2010.	64
FIG. 5. MAE and RMSE for total precipitable water calculated with GPS-IPW over the experiment period for NCEP model analyses.	66
FIG. 6. MAE and RMSE for total precipitable water calculated with GPS-IPW over the experiment period for WRF model analyses.	67
FIG. 7. MAE and RMSE for total precipitable water calculated with GOES-13 Sounder Ma retrievals over the experiment period for WRF model analyses.	68
FIG. 8. MAE and RMSE for total precipitable water calculated with GOES-13 Sounder Ma retrievals over the experiment period for NCEP model analyses.	69
FIG. 9. A comparison of NCEP and WRF model total precipitable water analyses all valid at 00 UTC 8 October 2011.	70
FIG. 10. A comparison of WRF model total precipitable water 12, 24, and 36 hour forecasts all valid at 00 UTC 8 October 2011.	72
FIG. 11. MAE and RMSE for total precipitable water calculated with GPS-IPW over the experiment period for WRF model 12-hour forecasts.	73
FIG. 12. MAE and RMSE for total precipitable water calculated with NAM analyses over the experiment period for WRF model 12-hour forecasts.	74

FIG. 13. MAE and RMSE for total precipitable water calculated with NAM analyses over the experiment period for WRF model 24-hour forecasts.	75
FIG. 14. MAE and RMSE for total precipitable water calculated with NAM analyses over the experiment period for WRF model 36-hour forecasts.	76
FIG. 15. MAE for relative humidity at 700 hPa and 850 hPa calculated with NAM analyses over the experiment period for WRF model 12-hour forecasts.....	77
FIG. 16. The total precipitable water analysis valid at 00 UTC 10 November 2011 from the NAM.	78
FIG. 17. The total precipitable water analysis valid at 00 UTC 10 November 2011 from the WRFX control run and a difference between the WRFX and NAM analyses for the same time.....	79
FIG. 18. The total precipitable water analysis valid at 00 UTC 10 November 2011 from the WRFZ experiment run and a difference between the WRFZ and NAM analyses for the same time.	80
FIG. 19. The 700 hPa relative humidity analysis valid at 00 UTC 10 November 2011 from the NAM.....	81
FIG. 20. The 700 hPa relative humidity analysis valid at 00 UTC 10 November 2011 from the WRFX control run and a difference between the WRFX and NAM analyses for the same time.	82
FIG. 21. The 700 hPa relative humidity analysis valid at 00 UTC 10 November 2011 from the WRFZ experiment run and a difference between the WRFZ and NAM analyses for the same time.	83
FIG. 22. The 850 hPa relative humidity analysis valid at 00 UTC 10 November 2011 from the NAM.....	84
FIG. 23. The 850 hPa relative humidity analysis valid at 00 UTC 10 November 2011 from the WRFX control run and a difference between the WRFX and NAM analyses for the same time.	85
FIG. 24. The 850 hPa relative humidity analysis from the WRFZ experiment run valid at 00 UTC 10 November 2011 and a difference between the WRFZ and NAM analyses for the same time.	86
FIG. 25. The total precipitable water analyses valid at 12 UTC 8 October 2011 from the WRFX and WRFZ.	87

FIG. 26. The total precipitable water analysis valid at 12 UTC 8 October 2011 from the NAM, a difference between the WRFX and NAM analyses, and a difference between the WRFZ and NAM analyses.....	88
FIG. 27. The 12-hour accumulated precipitation valid ending at 00 UTC 9 October 2011 from the NCEP Stage II multi-sensor analysis, WRFX 12-hour forecast, and WRFZ 12-hour forecast.	90
FIG. 28. The NAM analysis of total sky cover valid at 00 UTC 12 October 2011.	92
FIG. 29. The auto-conversion limit as a function of temperature that is used in the CRAS.	93
FIG. 30. MAE for total sky cover over the period from 00 UTC 28 September 2011 to 00 UTC 8 October 2011, calculated for WRF default fraction.....	94
FIG. 31. MAE for total sky cover over the period from 00 UTC 28 September 2011 to 00 UTC 8 October 2011, calculated for WRF maximum fraction.	95
FIG. 32. The NDFD one-hour total sky cover forecast, CRAS 12-hour forecast of total sky cover, WRFX 12-hour forecast of total sky cover using the default calculation, and WRFX 12-hour forecast of total sky cover using the maximum-layer calculation all valid at 00 UTC 12 October 2011.	96

1. Introduction

Water vapor is an important molecule in our atmosphere which has a profound impact on the dynamics and physics of the fluid earth system. Accurately assessing magnitudes and gradients of moisture in the troposphere, especially in the boundary layer, is an ongoing challenge. While in-situ observational data from surface stations and radiosondes paint a partial picture of the moisture distribution in the atmosphere, information collected from weather satellites is the only way to determine short-term changes in water vapor on spatial scales under a few hundred kilometers.

Many of the earth's most significant weather phenomena are a consequence of temperature and moisture gradients. The tropics and middle latitudes contain a substantial amount of water vapor, which condenses to produce clouds and precipitation. In order to better forecast the broad spectrum of diabatic weather processes, it is necessary to improve understanding of such processes on multiple spatial and temporal scales, from mesoscale convective systems (MCSs) to synoptic-scale mid-latitude weather systems, through their simulated evolution in numerical weather prediction (NWP) guidance. Essential to accurately resolving and parameterizing these phenomena as part of a forecast is incorporating satellite observations of cloud and water vapor into numerical models. The consistent use of these observations in real-time model simulations has the potential to improve predictions of storms and precipitation, a claim which is investigated here.

Since 1992, the development of the dynamics and physics within the Cooperative Institute for Meteorological Satellite Studies (CIMSS) Regional Assimilation System

(CRAS) weather prediction model (<http://cimss.ssec.wisc.edu/cras/>) has been guided by the addition of satellite products into the assimilation pre-forecast. During the pre-forecast, cloud and precipitable water (PW) products from the twelve hours ahead of the initialization time are substantiated in the modeled atmosphere. These products are predominantly from the Geostationary Operational Environmental Satellites (GOES) Imager and Sounder due to their relative temporal frequency. Polar-orbiting satellites, such as those equipped with a MODerate resolution Imaging Spectroradiometer (MODIS), can also be used where temporal frequency can be sacrificed in place of increased spatial and spectral resolution. The goal of the CRAS has been to show forecast improvement when additional satellite data sets are added to the traditional in-situ observations (R. Aune 2011, personal communication). In recent years, however, other modeling systems have grown in popularity as the development of the CRAS slowed. Despite this, the use of CRAS output gradually expanded into dozens of National Weather Service (NWS) forecast offices between 2006 and 2011. Forecaster comments reveal that the CRAS output continues to have a positive impact in certain forecast situations.

In contrast to the CRAS, the Weather Research and Forecasting (WRF) model (<http://wrf-model.org/>) is a NWP model built from an increasingly popular collection of code for simulating atmospheric conditions at high spatial scales. The WRF model is a state-of-the-art mesoscale NWP tool which was developed to satisfy the needs of both operational forecasters in the field and atmospheric scientists in a research setting. This functionality allows the WRF model to be used both in scientific studies and for real-time

prediction. NWS field offices across the United States are increasingly reliant on output from the WRF Environmental Modeling System (EMS), an end-to-end distributable for running the WRF locally and producing output (<http://strc.comet.ucar.edu/wrfems/>).

Since the WRF has been widely adopted for forecast applications, with improvements to its dynamical cores and physical packages continuing through the present time, it is an ideal platform for observation impact studies because of the applicability to numerous real-time users. Obtaining a better solution via a more accurate set of initial conditions is a long-standing tenet of NWP mathematics. The CRAS pre-forecast methodology remains a viable source of initial conditions (ICs) which have been influenced with satellite data. This investigation quantifies the degree of improvement that the CRAS-produced ICs have in WRF simulations out to 36 hours during portions of the Northern Hemisphere fall months of September and October 2011, where there are a combination of both moist and dry regimes over the north central United States.

This paper will provide a summary of the current state of GOES Sounder radiance and retrieval assimilation in numerical models as a motivating factor for this research; the design of the experiment in seeking to quantify the impact of these retrievals on a regional-scale domain; an explanation of how satellite observations, in the form of retrievals, are assimilated into the CRAS; a description of the CRAS and WRF sky cover algorithms; and some results and comparisons between the WRF simulations, CRAS, and validating analyses and point observations for certain moisture fields. The objective is to develop a methodology for an effective, applicable study easily replicated in the field that confronts substantial forecast problems resulting from tropospheric moisture gradients which are inadequately resolved in NWP guidance at the current time.

2. Background of problem

The basic premise of NWP is that it is an initial value problem. In striving to attain the perfect forecast, there are several other factors which constrain the accuracy of the solution, including parameterizations and approximations within the model; schemes which use time-stepping to solve partial differential equations over a finite interval; atmospheric features occurring on spatial and temporal scales smaller than resolved by the model; limited observations to populate the initial analysis, particularly above the surface and away from land; the quality and accuracy of those observations and the representation of any observation errors during the assimilation process; and the boundary conditions on the perimeter of the domain which can force the solution for long-duration simulations. The United States' National Centers for Environmental Prediction (NCEP) operational models use numerous data sets consisting of in-situ and remotely sensed observations in building their analysis. However, some forecasters have indicated that moisture representation in the NCEP models is sometimes inadequate for forecasting mesoscale precipitation events (G. Mann 2011, personal communication).

To resolve this issue, additional moisture information was sought from unexploited earth-observing satellite instruments for incorporation into model simulations. Retrievals from the GOES-13 Sounder were chosen due to the limited amount of use during the current assimilation process in the NCEP operational models (Keyser et al. 2011). As of this writing, the North American Mesoscale (NAM; <http://www.emc.ncep.noaa.gov/?branch=NAM>) model and Global Forecast System (GFS; <http://www.emc.ncep.noaa.gov/GFS/>) model do use brightness temperatures from

the GOES Sounders (GOES-11 and GOES-13) over ocean as part of their radiance assimilation system. However, they do not use retrievals, nor do not use the GOES Sounder observations over land. The Rapid Update Cycle (RUC) model, which is transitioning to the Rapid Refresh (RR; <http://rapidrefresh.noaa.gov/>) model, does use PW retrievals, but only those over ocean from the GOES-11 Sounder.

Figure 1 shows the three water vapor weighting functions for a standard mid-latitude summer atmosphere at the central wavelengths sensed by the current series GOES Sounder and future GOES imager (Gunshor et al. 2011). These weighting functions are at terrestrial infrared wavelengths on the edge of the water vapor absorption spectrum. They indicate that under standard summertime conditions, near-surface water vapor is not observable by the Sounder, and water vapor observed by the Sounder at each wavelength comes from a fairly broad vertical tropospheric range, usually at least 250 hPa deep. In very dry atmospheres, lower-tropospheric and even near-surface distributions of moisture are discernible. Such environments are occasionally evident during the winter season across North America. In these regimes, it is not uncommon for fairly narrow weighting functions to peak on or near the surface.

It is worth noting that there are currently no plans to expand vertical resolution of moisture information through increasing observable wavelengths sensed by future imagers onboard operational geostationary satellites (Schmit et al. 2008). For example, the Advanced Baseline Imager (ABI) on GOES R-Series (GOES-R), the first satellite of which will be ready for launch in late 2015 (T. Schmit 2011, personal communication), will provide for a significantly higher temporal and horizontal resolution of clouds and water vapor, nominally 2 km at the satellite subpoint, but for still only three water vapor-

sensing bands at the approximate wavelengths as the current GOES Sounder (Schmit et al. 2008). This despite that there have been a number of studies which have described the benefits of hyperspectral infrared observations, and the likely resultant increased value such information would bring to short-term atmospheric predictability of high-impact weather phenomena via model simulations (Li et al. 2011).

a. Precipitation efficiency

While there remains a substantial disadvantage to our current geostationary earth-observing satellites' blindness toward low-level water vapor concentration, gradients, and evolution, all is not lost, though it does present a setback. Thunderstorms are responsible for vast amounts of precipitation over the United States, particularly during the summer. Market et al. (2003) investigated the precipitation efficiencies, the ratio of accumulated precipitation to PW, for MCSs over the central United States during the July through September periods of 2000 and 2001. PW fields from the RUC were used in concert with radar-derived precipitation grids to calculate precipitation efficiencies. Soundings from the GOES and winds from the RUC were applied in assessing the pre-MCS environment. After an analysis of the statistics, it was found that there was a strong positive correlation between precipitation efficiency and the relative humidity between the surface and lifting condensation level (LCL), and strong negative correlations between the precipitation efficiency and both the convective inhibition (CIN) based on the lowest 100-hPa parcel, and the layer wind shear across the convective, warm-cloud depth. There were statistically insignificant findings between precipitation efficiency and PW, warm cloud depth, and relative humidity through the warm cloud layer.

b. Conservation of enthalpy

Though Market's study was inconclusive in finding a correlation between precipitation efficiency and PW, theory provides a connection between temperature and moisture during convective processes. As convective towers ascend, the parcel cools and condenses resulting in a release of latent heat. In order to conserve moist enthalpy E ,

$$E = C_p T + L_v q,$$

where C_p is the heat capacity at constant pressure, T is temperature, L_v is the latent heat of vaporization, and q is specific humidity, not only does the convection require a removal of water vapor from the parcel, but that amount must be directly proportional to the change in temperature. This relationship must also hold for the depth of the convective cloud, from the base pressure at the LCL, C_{base} , to its top pressure at the equilibrium level, C_{top} , as shown in Baldwin et al. (2002), such that:

$$\int_{C_{top}}^{C_{base}} L_v \Delta q dp = \int_{C_{base}}^{C_{top}} C_p \Delta T dp$$

Therefore, the availability of middle and upper tropospheric moisture for deep convective processes is a factor in their strength, effectiveness, and longevity, because as environmental temperature increases aloft, the stability increases and parcel buoyancy decreases. In fact, it has been demonstrated that tropical convection is responsive to mid-level moisture, as found in Shepherd et al. (2001) and Thompkins (2001). This is also an observation which has been incorporated into the Kain-Fritsch (KF) convective scheme (Kain 2004), and further confirmed by Knupp and Cotton (1985), which found that environmental humidity is an important factor in assessing downdraft strength. The KF

scheme is the convective parameterization of choice in this study to allow the model solution to indicate increased sensitivity as a consequence of differential moisture resulting in vertical mass fluxes.

c. Advanced Research WRF configuration

The Advanced Research WRF (ARW) equations are fully compressible and cast in flux form as described in Skamarock et al. (2008). The configuration is non-hydrostatic for experiments conducted in this study. The vertical coordinate is terrain-following and based on dry-hydrostatic pressure with a constant pressure surface at the top of the model. A horizontal Arakawa C-grid staggering is applied with a third-order Runge-Kutta time integration scheme. In the ARW's moist Euler equations, there are no moisture source terms in the mass conservation equation. The dry air mass remains coupled to the prognostic variables, momentum, potential temperature, geopotential, pressure, and inverse density, with the conservation equation for dry air guiding the solution. The moist equations, as shown in Skamarock et al. (2008), assume the form:

$$\begin{aligned}
 \partial_t U + (\nabla \cdot \mathbf{V}u) + \mu_d \alpha \partial_x p + (\alpha/\alpha_d) \partial_\eta p \partial_x \phi &= F_U \\
 \partial_t V + (\nabla \cdot \mathbf{V}v) + \mu_d \alpha \partial_y p + (\alpha/\alpha_d) \partial_\eta p \partial_y \phi &= F_V \\
 \partial_t W + (\nabla \cdot \mathbf{V}w) - g[(\alpha/\alpha_d) \partial_\eta p - \mu_d] &= F_W \\
 \partial_t \Theta + (\nabla \cdot \mathbf{V}\theta) &= F_\Theta \\
 \partial_t \mu_d + (\nabla \cdot \mathbf{V}) &= 0 \\
 \partial_t \phi + \mu_d^{-1} [(\mathbf{V} \cdot \nabla \phi) - gW] &= 0 \\
 \partial_t Q_m + (\nabla \cdot \mathbf{V}q_m) &= F_{Q_m}
 \end{aligned}$$

for a three-dimensional coupled (via scalar multiplication with dry hydrostatic pressure difference μ_d) velocity vector \mathbf{V} with components U , V , and W , conventional components

of velocity u , v , and w , pressure p , geopotential ϕ , coupled potential temperature Θ , conventional potential temperature θ , gravity g , coupled generic mixing ratios Q_m , conventional generic mixing ratios q_m , and forcing terms F .

In these equations, α is the inverse full parcel density. The inverse full parcel density, which contains the reciprocal of the sum of the product of dry air density with the model water species mixing ratios and unity, is a coefficient to the pressure gradient terms and horizontal geopotential gradient terms. In addition, each moisture species has an advective component and time tendency equal to the forcing term. This formulation also uses a diagnostic relation for the full pressure expressed by

$$p = p_0 \left(\frac{R_d \theta_m}{p_0 \alpha_d} \right)^\gamma,$$

where p_0 is the reference sea-level pressure, α_d is the inverse density of dry air, θ_m is the moist potential temperature, R_d is the gas constant for dry air, and γ is the ratio of heat capacities for dry air at constant pressure and volume.

Early versions of the ARW dynamical core met some criticism for the use of Runge-Kutta transport integration with a flux divergence operator that was conservative but did not assure positive definiteness. Positive definiteness of moisture variables is a natural physical constraint (i.e., negative mixing ratios are not permissible) that is not necessarily easily enforced in a finite-difference time-stepping algorithm. Recent versions of the ARW dynamical core, used in experiments conducted here, have additional capabilities which apply a positive-definite flux renormalization to conclude the Runge-Kutta transport (Skamarock et al. 2008). The scheme and effect on the model solution is explained in Skamarock and Weisman (2009).

FLUX RENORMALIZATION

The application to the problem at hand in these experiments is evident. Prior to developing a scheme that enforced positive definiteness of the moisture variables, water mass was not a conserved property. Skamarock and Weisman (2009) were able to demonstrate that the use of a flux renormalization, also known as a positive-definiteness limiter, had sizable positive impact on precipitation forecasts, though it did not eliminate the positive bias to ARW precipitation forecasts. Without the renormalization, liquid cloud water was a substantial contributor to artificial, numerically-generated moisture. While the WRF provides configurability to force negative quantities of the moisture to zero, this correction leads to an increase in the mass of water, both of that species and the species-summed, total quantity.

While Skamarock and Weisman (2009) focused on the influence of flux renormalization to precipitation resulting from explicit convection, the findings are relevant to the simulations conducted as part of this study despite the use of a convective parameterization with larger grid spacing than adequate for explicit convection. However, convective parameterizations are the numerical forcing behind the precipitation when they are applied. Parameterizations are designed to inhibit numerical, unphysical instability in the model, not accurately produce precipitation.

Furthermore, flux renormalization does not resolve all sources for moisture error within the model. Skamarock and Weisman (2009) introduced a process which conserves water mass at each species instead of the total, summed quantity. The result of this is that phase changes may be artificially limited despite the fact that the total water

mass is conserved. In addition, each scalar moisture quantity is advected independently and there is no articulated constraint within the dynamical core that connects the scalar moisture variables. As such, the moisture budget, and consequently, the entropy budget are not without lingering sources for error. Mixing parameterizations also bear some responsibility to the precipitation bias (Skamarock and Weisman 2009).

CONVECTIVE SCHEME

The WRF simulations in this experiment all utilize the KF convective parameterization, which is a mass flux scheme, and thus requires an adjusted response based on the grid scaling. The closure for the KF scheme is convective available potential energy (CAPE). This is an important source for latent heat release, and thus, accumulated convective precipitation. It has been shown in Kain and Fritsch (1990) that the normalized vertical mass flux varies significantly—by a factor of two—in the upper troposphere for changes of relative humidity between 50% and 90%. This sensitivity is critical because, for cold temperatures, the amount of water vapor mixing ratio required to adjust the relative humidity is not particularly substantial.

3. Data and methodology

The configuration of the models in this WRF transition experiment was intended to be easily duplicated in the field as part of the EMS. The dynamics core and physics packages chosen for the ARW runs closely match those from the local WRF model used at that NWS office in Milwaukee, Wisconsin. Table 1 outlines the core configuration. The WRF code used for simulations throughout the study was version 3.1.1.

The domain selected for the simulations was over the north central United States, including the Northern Plains and Upper Mississippi Valley. The Lambert Conformal grid contained 100 grid points in each horizontal direction with equal-area spacing of 20 km to minimize the time to complete each simulation. The domain was thus square with 2000 km on each boundary and 45 vertical levels up to a model top of 50 hPa. The WRF model runs were initialized twice daily during the experiment period at the standard times of 00 and 12 UTC and executed out to 36 hours, outputting every hour.

a. Configuration of control and experimental WRF runs

There was one control and two experimental WRF runs, all of which utilized a MODIS sea surface temperature composite for water grid points (Haines et al. 2007) and soil moisture from the operational 0.5-degree GFS distributed by NCEP. Soil temperatures and the source of atmospheric properties were different based on the run. Temperature, wind, relative humidity (water vapor mixing ratio), cloud water mixing ratio, geopotential height, and surface pressure were pre-processed by the WRF prior to each unique model simulation. Additional moisture information was available for the first experimental run (WRFY). As part of the WRF preparation process, input model fields were interpolated both vertically and horizontally to the WRF grid, which resulted in some minor smoothing to the analysis.

The control run, herein referred to as WRFX, contained ICs and boundary conditions (BCs) from the GFS executed six hours prior to the experiment initialization time. Thus, the six-hour forecast from the GFS was used to initialize the WRFX run. Lateral boundaries were forced every three hours from the same GFS run. Moisture

components of the GFS initial and boundary conditions were relative humidity and cloud water mixing ratio.

The first experimental run, herein referred to as WRFY, contained ICs and BCs from a CRAS simulation run on an expanded 45 km grid with an identical projection, allowing lateral boundaries to be forced hourly. Moisture initialization in the WRFY came from four mixing ratios produced by the CRAS pre-forecast procedure: water vapor, cloud water, ice water, and rain water. The CRAS utilized only one cloud mixing ratio and one precipitation mixing ratio, however. The form of the water carried in the CRAS mixing ratio arrays was a function of the temperature. They were classified prior to being served to the WRF preparation process as input. The background for the CRAS simulation was the same GFS run as used in the WRFX run.

The second experimental run, herein referred to as WRFZ, used the ICs from a “cold start” CRAS initial-hour assimilation but BCs from the previous GFS run, as in the WRFX. Like the WRFX, the WRFZ used a six-hour forecast from the GFS as the IC background. The WRFY took advantage of the CRAS pre-forecast assimilation of GOES Sounder retrievals into the ICs, which is commonly known as a “hot start”. The WRFZ took advantage of the Sounder retrievals which improve the moisture analysis only at the initialization time. Moisture initialization in the WRFZ came in the form of water vapor mixing ratio only.

The purpose and configuration of the WRFZ run was strictly to assess whether the updated moisture analysis would have an impact on short-term forecasts of moisture-related variables: relative humidity, total precipitable water (TPW), and accumulated precipitation. In contrast, the intent of the WRFY experiment was to see whether the

CRAS could build an analysis which could outperform a simple assimilation technique, or no assimilation at all, since the CRAS was developed to assess the impact of space-based observations on the accuracy of NWP solutions. Producing forecasts using parameterizations and techniques which exploit and give merit to information from satellites, particularly the GOES Sounder, was thus a necessary component of the project.

b. Building analysis from GOES Sounder retrievals with CRAS

The CRAS pre-forecast procedure contained a 12-hour spin-up forecast to initialize water vapor and clouds from the GOES Sounders. The retrieved cloud and water vapor mixing ratios were inserted into the spin-up at the median time of the Sounder scan. CRAS physics and dynamics were run following each insert. The iterative process physically instantiated the retrievals in the modeled atmosphere. The CRAS uses a semi-implicit time stepping scheme described by McGregor et al. (1978) with a third-order time filter (Raymond 1991). The advective form of the motion equations follows Leslie et al. (1985) with horizontal moisture and precipitation advection included. In lieu of horizontal diffusion, a sixth-order tangent filter is applied (Raymond 1988) to preserve horizontal gradients.

While not the emphasis of this study, the CRAS dynamical and physical schemes must be considered in light of their role as ICs and BCs for the WRFY experimental run. The CRAS modifies the background for the retrieval assimilation during the pre-forecast spin-up used prior to the initialization of the WRFY. A modified Kuo convective parameterization is used in the CRAS (Raymond and Aune 2003). Cloud is distributed between the base and top as defined by the environmental static stability. Only deep

convection is parameterized. There is no moistening of the column due to deep convection, and no shallow convective scheme. Non-convective sub-layers are used as the moisture source for subsequent convection. The explicit cloud and precipitation microphysics follow Raymond (1995) with phase diagnostics from Dudhia (1989). Sundquist (1989) articulates the collision-coalescence, precipitation, evaporation, and auto-conversion methodologies. The relative humidity limits for cloud evaporation are a function of temperature, with cloud condensation allowed for relative humidity values of less than 100% in the boundary layer. Single-layer cloud fields are the result of a non-local turbulence scheme with vertical turbulence exchange derived from a K-theory method with a turbulent kinetic energy parameter. Liquid cloud sedimentation is from Lee (1992) and ice cloud sedimentation follows Heymsfield and Donner (1990). The CRAS model is pseudo-non-hydrostatic with parameterized rain drag (Raymond and Aune 1998).

Besides cloud retrieval products which build or clear cloud mixing ratios in the model domain, there are three disjoint layer-integrated tropospheric PW products from the GOES Sounders. They correct the water vapor in the model during the pre-forecast procedure. At the end of the spin-up, the initial time of the simulation, the six-hour forecasts of temperature and wind from the operational GFS run six hours prior to the start time are merged with the result of the moisture assimilation. There is no adjustment made to the background grid points not observed by the Sounder. For example, there is no GOES Sounder coverage for some Canadian portions of the experiment domain. For the WRFY, it is possible for upstream GOES Sounder observations to influence the solution during the model execution due to an expanded CRAS parent domain.

c. Summary of methodology behind GOES Sounder moisture retrievals

The procedure which builds the retrieved parameter for a clear field of view out of the raw GOES Sounder observations is described in Li et al. (2008). The full retrieval algorithm consists of a regression component and a physical component. Prior to the enhancements by Li et al. (2008), a NWP model forecast profile was used as the sole first guess for the physical iterative approach. The linear regression procedure developed by Li et al. (2008), to produce the herein referred to as Li retrievals, used three primary predictors: brightness temperatures, forecast profiles, and surface temperature and moisture observations. The nonlinear physical algorithm closely followed Ma et al. (1999), the legacy procedure for extracting quantitative water vapor information from infrared radiances into the herein referred to as Ma retrievals. There were some changes, however. Beyond the iteratively-developed temperature and moisture profiles, Li et al. (2008) produced a training database consisting of collocated radiosonde observations, GOES-12 brightness temperature measurements, and GFS model profiles for a period from June 2003 through September 2004 that was used to create two covariance matrices, one for the regression and the other for the forecast. This training database was also used to reduce the bias between the observed radiance and the calculated one. The cumulative result of the changes is better, less-biased TPW Li retrievals to the amount of 0.4 mm compared to the legacy Ma retrievals (Li et al. 2008).

d. Incorporation of the clear retrieval into the model-simulated atmosphere

For a clear-sky Sounder retrieval within the CRAS model domain, water vapor adjustments are performed using the background. As part of this process, cloud is

removed from the pre-forecast analysis if present. If not, the mean background mixing ratio profile is calculated and the perturbations are removed but retained. Subsequently, a strong constraint, one-dimensional variational method adjusts the mean profile using the power function approach from Smith (1966) to match the water vapor mixing ratio from the GOES Sounder PW retrieval. Then, the perturbations are added back into the adjusted profile. During this procedure, relative humidity at any one level within the layer is not forced beyond 95% in order to assure clouds do not immediately develop in the model and thus enforce the clear-sky condition required to make the retrieval. This method is beneficial to retain the structure of the temperature profile and lapse rates.

e. History of the approach

Incorporating remotely-sensed retrievals of PW into numerical analyses and prediction systems was first demonstrated in the early 1990s. Kuo et al. (1993) developed an analytic relaxation scheme for assimilating TPW retrievals from ground-based profilers. In 1994, Filiberti et al. demonstrated positive results with assimilated TPW retrieved from the Special Sensor Microwave/Imager (SSM/I) radiometer using a one-dimensional optimal interpolation technique. That technique involved a statistical constraint on the model while updating the vertical moisture profile from the analysis as a result of the SSM/I observation. Because PW is an integrated quantity, the methods in Kuo et al. (1993) and Filiberti et al. (1994) required a background vertical moisture profile that was revised with the retrieved estimate. This was a philosophy first explained in Gal-Chen et al. (1986) for improving temperatures in NWP analyses from satellite retrievals.

The mid-1990s led to the first assimilation studies involving retrieved properties from GOES instruments. Vertically integrated moisture retrieved from observations taken with the Visible/Infrared Spin Scan-Radiometer (VISSR) Atmospheric Sounder (VAS) on GOES-7 was among the first derived quantities suggested for inclusion as part of a numerical model's pre-forecast construction (Aune 1994). Starting with the Sounder on GOES-8, three separate PW retrievals were possible at a nominal 10 km resolution courtesy of three water vapor channels. The specification of the GOES Sounder has not changed since then. Sounder retrievals are generally available hourly. In order to assimilate this water vapor information into the CRAS, it was necessary to develop an approach that maintained the integrity of background vertical moisture gradients while adjusting the bulk properties observed by the GOES instruments. Particularly important in this process was the realization that, for some tropospheric water vapor concentrations, the origin of water vapor emission observed by the sensor is in the middle and upper troposphere.

f. Assimilation procedure

With the GOES Sounder still operational today, the assimilation strategy developed for the CRAS is still a formidable method today. Prior to the beginning of the PW retrieval assimilation process, an analysis is obtained from a previous model run, which depends on the length of the pre-forecast assimilation. For the WRFY, the first analysis in the pre-forecast is from the operational GFS run initialized 12 hours prior to the start of the simulation. The WRFZ uses the six-hour forecast from the operational GFS run six hours prior to the start of the WRFZ. The pre-forecast atmosphere from the

GFS is treated as an analysis and serves as the background for the GOES PW retrieval. It is possible to approximate a mean profile of mixing ratio from this model background, using a power function approach described by Smith (1966). With the Smith approach, the mean mixing ratio at a pressure level, p , is calculated from a surface pressure, p_0 , and background surface mixing ratio, w_B ,

$$\overline{w(p)} = w_B \left(\frac{p}{p_0} \right)^\lambda,$$

where λ is an integer between 1 and 3. The exponent, λ , is incremented by one until the PW background, PW_B , is proportional to the column-integrated quantity consisting of mean water vapor at each pressure level. The bounds of integration are dependent on the depth of the retrieval. During three-layer PW assimilation, as used in this experiment, the integration is bounded between sigma levels in the CRAS as determined from the layer of the retrieval: 1 to 0.9, 0.9 to 0.7, and 0.7 to 0.3. Layers are processed starting with the the lowest sigma layer and ending with the upper sigma layer. For each of these three sigma layers, the mean mixing ratio profile is removed from the background but retained for a subsequent adjustment. The result is a profile of mixing ratio perturbations to be reapplied following the adjustment.

The retrieved values are brought to populate the model grid using the recursive filter analysis (Hayden and Purser 1995). Such an analysis combines multiple retrievals near a model grid point where the grid spacing is greater than the retrieval density. A local quality check is performed within each grid cell to identify outliers, which are omitted from the sample. In addition, observations are omitted when the difference between the background surface pressure and the retrieval surface pressure is greater than

10 hPa. The background mean mixing ratio profile is then updated based on an adjustment of λ in the previous equation to achieve a balance, $\overline{PW_B} = PW_{GOES} - \overline{PW_B'}$, between the mean background integrated PW, $\overline{PW_B}$, and the difference between the bounded and averaged quantity PW_{GOES} from the retrievals and the mean background perturbation PW, $\overline{PW_B'}$. To complete the assimilation, the perturbation mixing ratios are added to the adjusted mean mixing ratio profile. Then, a quality check is performed to assure there is no saturation. Any residual moisture is transferred to the top of the bounded layer for use in the subsequent layer calculation. To this end, the purpose of applying this method is to increase or reduce moisture unilaterally over the entire profile, and not to alter vertical moisture gradients already present in the model.

g. Critique on likelihood of success

This method does not evade criticism. Unlike most multi-dimensional variational approaches, this one-dimensional approach does not consider systematic or random error in the observations or the model forecast. While good, Li et al. (2008) demonstrated that the retrievals are not without bias. Weather model forecasts are not improved as a result of assimilating additional observations where the random error of those observations is more than the a priori bias in the background forecast (Gutman et al. 2004). Without this consideration, it may be difficult to expect an improvement from the assimilation. In addition, this technique does not necessarily preserve horizontal gradients of retrieved PW outside of the recursive filter used to combine multiple retrievals in close proximity. Still, there is no redistribution of moisture between adjacent grid points which would purport a water vapor mass conservation constraint over a fixed area. This would be

difficult to implement on a regional model, however, because mass fluxes exist at the boundaries where the budget would be essentially uncontrolled.

Considering this, it is appropriate to speculate that this assimilation process may be better for model grid point spacing distances larger than the retrieval density. A larger extent of the filter typically results in a smaller impact of random error during the assimilation since more retrievals would produce the mean profile. Still, this logic is not straightforward because numerical artifacts in the model, such as finite differencing formulations which incorporate diffusion, and other parameterizations which assure numerical stability, work to smooth the model solution, particularly for features with local minima or maxima covering a small number of grid points, over a fairly short period following the time of assimilation, at or before the analysis.

The GOES-13 Sounder moisture retrieval correction can be seen in Figure 2, which compares the model background at WRFX initialization time to a radiosonde sounding from International Falls, Minnesota, (KINL) at 12 UTC on 13 November 2011, and Figure 3, which compares the retrieval-adjusted profile to the same KINL sounding. In this case, the retrieval adjusts the moisture profile much closer to the observation than the background. The primary adjustment to the moisture profile occurs in the middle and upper troposphere where the Sounder weighting functions peak. There is no change to the temperature or momentum field as part of the assimilation scheme.

h. Adjustments due to cloudy fields of view

The assimilation of clouds into the pre-forecast was first demonstrated in Aune (1996) and follows the approach from Bayler et al. (2000) in this study. There are two

GOES Sounder products that are part of the cloud assimilation scheme: Cloud Top Pressure (CTP) and Effective Cloud Amount (ECA). The ECA is an indicator of the amount of cloud mass to add to the model grid. Clouds pre-existing in the model are left unmodified if the CTP concurs with their horizontal and vertical placement. For a cloudy background where the cloud height is lower than the retrieval CTP, the cloud is adjusted to match the height from the Sounder retrieval. Modeled clouds at a height greater than the retrieval CTP are cleared. When the background is clear in the presence of an observed cloud, the relative humidity is adjusted and a new cloud deck is built consistent with the CRAS cloud physics.

i. Experiment domain and justification

The domain selected for the experiment contains GOES-13 Sounder input for the United States grid points, and adjacent points in Canada approximately south of 50 degrees North latitude. The intent is to capture the consequence of resolved moisture gradients, requiring numerous clear fields of view from space, in weak zonal or southerly flow, typical of summertime and early fall mid-latitude patterns. Northerly winds typically introduce cool, dry, and stable air into the northern United States, so potential for notable impact in these regimes is not anticipated, especially without Sounder coverage in the far northern portion of the grid. Weaker winds are also ideal for this simulation so that the BCs do not control the solution early in the simulation. A winter-characteristic strong 200-knot jet streak will overtake the entire grid in less than six hours. For a mean flow speed of 20 knots, the domain is completely forced by boundary conditions after around 55 hours of simulation. However, deep moisture is traditionally

observed in the early and mid summer. Thus, water vapor weighting functions at the wavelengths sensed by the GOES Sounder are likely to peak higher in the troposphere than in the late summer and early fall, when drier air filters out of Canada.

j. Initial evaluations

The initial investigation on this domain was to assess the consequence of different moisture analyses on precipitation predictions, especially when strong convective elements were involved. To show this, a series of six WRF simulations were initialized at 00 UTC 31 August 2010 in the basic ARW configuration explained previously, with the exception of a five-layer thermal diffusion method as the land-surface scheme. Five of the simulations contained initial and boundary conditions from the GFS. Three of those simulations had relative humidity modified to 90% of the outputted value in one layer for both the ICs and BCs: surface to 800 hPa, resulting in a layer mixing ratio decrease of approximately 1.25 g/kg in the ICs, 750 to 400 hPa, resulting in a layer mixing ratio decrease of approximately 0.30 g/kg, and 350 to 100 hPa, resulting in a layer mixing ratio decrease of 0.01 g/kg. One of the simulations contained 90% of the relative humidity from GFS initial conditions across the entire depth of the atmosphere, an entire atmosphere average mixing ratio decrease of 0.23 g/kg in the ICs. The fifth simulation contained the GFS initial conditions with no change. The sixth simulation was from the CRAS. BCs were forced every three hours out to the 36-hour simulation length.

Figure 4 shows the comparison of the 36-hour accumulated precipitation between these model runs. Note the difference in the amounts between the GFS simulations despite the same coverage pattern. The most sizable impact in the precipitation forecasts

came from the decrease in the initial water vapor in the lower levels of the GFS. However, the decrease in mid-level moisture also played a prominent role in decreasing precipitation amounts. Even the relatively insubstantial change to the upper tropospheric water vapor decreased surface convective precipitation along the southern extremity of the precipitation band. The overall, mean-relative distribution of the precipitation is the same among all of the GFS runs. However, the CRAS simulation suggests the maximum in precipitation over a different area than the GFS. Precipitation output from NWP models is traditionally spatially distributed and lacking in sharp, reliable definition, because, as in this case, convective precipitation falls as the result of parameterizations which keep the model numerically stable.

4. Precipitable water results

In assessing the value of the GOES-13 Sounder retrievals to the WRF forecasts, it was first necessary to examine the improvement to the PW analyses initializing the model runs. Not only was the error of the control compared to the experiment, but the NCEP operational models were verified against point observations as well as GOES-13 Sounder PW retrievals. The subsequent evaluation focused on the impact of the retrievals on forecasts, in 12-hour increments, through 36 hours, for each of the simulations, the control and both experiments. There were several fields that were examined in the latter portion of the evaluation: 12-hour accumulated precipitation compared against the NCEP Stage II precipitation analysis, 700 hPa and 850 hPa relative humidity compared against the NAM analysis, total sky cover compared against the National Digital Forecast Database (NDFD) 1-hr forecast and NAM analysis, and TPW compared against the

NAM analysis and point Global Positioning System (GPS) integrated precipitable water (IPW) observations. For comparisons involving NAM mass fields (relative humidity, TPW, and sky cover), statistics were computed for grid points within the interior of the domain; for those involving the NDFD, statistics were computed for grid points within the continental United States in the interior of the domain; for those involving GPS-IPW, statistics were computed for TPW at grid points near the observation sites; and for those involving the Stage II analysis, precipitation verification was computed for interior grid points observable by the United States' Weather Surveillance Radar 88 Doppler (WSR-88D) network. In figures containing maps, the spatial coverage of verification for that specific variable and observing platform is outlined in red. Interior grid points were used for the grid verification of the model domain instead of all eligible grid points to discount any BC and WRF blend zone influences from the results. The Model Evaluation Tools (MET) package, version 3 (<http://www.dtcenter.org/met/users/>), was used to compute the statistics. The primary statistics used to assess performance were mean absolute error (MAE) and root-mean-square error (RMSE).

The evaluation period consisted of 21 times between 00 UTC on 28 September 2011 and 00 UTC on 8 October 2011. This period was chosen for both dry and moist regimes. In addition, most precipitation was the result of well-forced, kinematic processes rather than thermodynamically driven. The objective was to establish whether a remotely sensed, integrated quantity could be adequately analyzed to a three-dimensional grid and produce favorable results in short-term forecasts, under 36 hours.

The growth of the GPS constellation of navigation-aiding satellites has spurred a unique approach to assessing atmospheric water vapor for verification purposes. GPS

satellites transmit radio signals to receivers on the ground. This signal is disturbed by moisture concentrations in the troposphere. This phenomenon, known as “wet delay”, has been found to be nearly proportional to the IPW between the satellite transmitter and the receiver (Askne and Nordius 1987). The transformation from “wet delay” into an estimate of PW is explained in Duan et al. (1996). Duan et al. (1996) compared the accuracy of the transformed GPS “wet delay” calculations to measurements from a water vapor radiometer during a May 1993 field campaign in the Southern Plains. The observations suggested that the GPS-IPW technique estimated water vapor with a RMSE of 1.0 to 1.5 mm. Duan et al. (1996) commented that there are theoretical cases in which the error of GPS-IPW estimates may prove larger, but these situations, which involve concentrations of large water-coated, ice particles, occur infrequently in nature.

a. Error of NCEP operational model analyses compared to GPS-IPW

The first assessment was a comparison of the TPW MAE among the NCEP operational models when validated with GPS-IPW observations: the NAM, RUC, and GFS. The MAE was calculated based on approximately 70 GPS-IPW sites within the domain. The sites used for each verification time varied due to availability of the observation, and were not equidistantly or randomly spread across the grid. There were portions of the verification domain where the GPS-IPW observation network was denser. It is possible that the GPS-IPW results may be geographically biased to certain regions and cities. For example, the state of Michigan has around 25 functioning GPS-IPW sites. Each GPS-IPW observation was compared to the nearest grid point. In this comparison, it was found that the NAM had a lesser mean MAE than the RUC and the GFS had the

highest MAE. Table 2 contains the mean MAE and RMSE for the three operational NCEP models. Figure 5 shows the trend in performance based on MAE and RMSE over the experiment period. In general, the NAM MAE was less than the other two models for all but three of the 21 evaluation times. That is, the NAM had the lowest MAE compared in this fashion for 86% of the times. This result was not surprising because the NAM and RUC both assimilate GPS-IPW measurements, while the GFS does not.

b. Error of experiment and control WRF analyses compared to GPS-IPW

Another investigation calculated the mean TPW MAE for the experimental runs compared against GPS-IPW during the evaluation period. There was not a discernible leader, as indicated in the mean MAE and RMSE over the period shown in Table 3. The difference in mean MAE over this period between the best performer, the WRFX (control), and the WRFY was 0.03 mm. The WRFY had the lowest MAE for 38% of the 21 periods; the WRFZ had the lowest MAE for 33% of the periods; and the WRFX had the lowest MAE for 28% of the periods, as shown in Figure 6, which also indicates a similar trend in the run-to-run RMSE during the experiment period. The inconclusive results were likely due to the poor spatial heterogeneity of GPS-IPW sites across the domain compared to the magnitude of the correction. Because of this, it is possible that some horizontal moisture distributions favor one analysis over the others.

c. Error of experiment and control WRF analyses compared to GOES-13 retrievals

A second comparison was done computing the TPW MAE for analyses against the GOES-13 Sounder Ma retrievals using the same methodology as described previously for point-wise comparisons. Ma retrievals in clear fields of view were used in the

comparison; there was no comparison conducted in cloudy fields of view. Furthermore, the GOES Sounder does not scan above approximately 50 degrees North latitude, so the majority of verified grid points were within the United States. The result of this method was that greatest errors were likely to occur in locations where a PW retrieval was made in clear sky but the nearest analysis grid point was cloudy. This was an acceptable procedure because, despite weaknesses for low clouds and thin high clouds, the GOES Sounder observations have been heavily utilized to assess whether cloud exists in the creation of cloud-related products (Schreiner et al. 2002). In this case, it was found that the WRFZ had the lowest mean MAE compared to the WRFX and WRFY. Table 4 contains the mean MAE and RMSE calculated for the WRF runs using the retrievals as truth. Figure 7 shows the run-to-run trend in the MAE and RMSE over the experiment period. The WRFY and the WRFZ contain GOES-13 Sounder Li retrievals in clear fields of view. This statistic confirms that the Sounder retrievals are assimilated into the experimental runs. It also indicates that, if the GOES Sounder retrievals are more accurate than the GFS background, then the WRFZ analysis, in general, is more accurate than the WRFX (control). Ongoing research indicates that over the experiment period, for all retrievals, even those outside the experiment domain, compared to GPS-IPW observations, the GOES Sounder Li and Ma retrievals exhibited more bias than the GFS background analysis (G. Wade 2011, personal communication).

It is not surprising that the mean TPW MAE is not closer to zero, because there were differences between the assimilation method and the comparison. Beyond the difference in technique between the Li retrievals assimilated in forming the WRFY and

WRFZ analyses and the Ma retrievals used as truth in the comparisons, the assimilated Li retrievals were averaged around each grid point, whereas during the comparison to calculate MAE, each retrieval was compared against the nearest grid point. Furthermore, for grid points near both cloudy and clear retrievals, the adjusted profile may have contained both retrieval cloud and water vapor influences. Such a profile may be starkly different in water vapor content to a nearby clear field of view retrieval which is compared against it, which would increase the error. Lastly, there is a slight loss of precision to integrated quantities such as TPW when the WRF runs are initialized with pressure surfaces in composing the initial tropospheric state because layers are derived from interpolation between levels. This tends to lead to a smoothing of atmospheric moisture profiles in the vertical dimension depending on the depth between pressure surfaces in the ICs.

d. Error of NCEP operational model analyses compared to GOES-13 retrievals

In conducting point-wise comparisons between Ma PW retrievals from the GOES-13 Sounder and model grid points, it was found that the GFS had the lower mean MAE during the evaluation period, whereas the RUC had the highest. The same methodology was used as discussed previously. In this comparison, however, the GFS initialization had the lowest MAE only 57% percent of the time during the period. The trend of MAE and RMSE for the NCEP operational model analyses over the experiment period is shown in Figure 8. The absolute difference between the GFS and NAM mean TPW MAE was only 0.07 mm with the Ma retrievals as truth, compared to 0.39 mm for the GPS-IPW comparison, where the NAM analysis showed less error against the GPS-

IPW network. Mean MAE and RMSE values for the NAM, RUC, and GFS, are shown in Table 5. The TPW MAE of the GFS appeared to outperform the NAM and RUC when there were more clear-sky retrievals available for comparison. That is, the GFS MAE was the lowest of the models involved in the comparison when the verification contained a smaller fraction of cloudy observations than clear fields of view. As a general trend for all models compared, their TPW MAE was lower when the domain was clearer and thus likely drier.

The better GFS performance is explainable because the GFS was used as the first guess for the GOES-13 Sounder retrievals. However, the GFS analysis used for the retrieval background was not from the same GFS run it was verified against. This allows the possibility that the previous forecast was used as a background for the subsequent GFS run, and thus was producing desirable results for the GFS overall and a discrepancy compared to the GPS-IPW results verifying the same quantity for the operational models.

e. Case study

The analyses from 00 UTC 8 October 2011 are shown in Figure 9. In all analyses, the position of the presumed frontal structure across the Northern Plains was almost exactly the same. The WRFZ analysis was less smooth than the other analyses due to the individual disparities between spatially close retrievals. The moisture assimilation does not change the momentum fields, so the kinematics in the WRFX and WRFZ were the same at the analysis time. Momentum fields from the CRAS may have modified the WRFY prediction beyond the analysis (initialization) time, which is the last time the GFS wind fields are merged with the pre-forecast spin-up. The comparison

between the WRFX and WRFZ analysis indicates that the result of the retrieval assimilation was to increase moisture across central Oklahoma and eastern Kansas, and slightly decrease moisture in Minnesota and far southwestern Ontario. A look at Figure 10 shows how TPW forecasts for that analysis time developed with subsequent model runs and the inclusion of the GOES Sounder moisture retrievals. The WRFX and the WRFZ have the same boundary conditions, so it was expected that the 36-hour forecasts would be approximately the same. In this case, the 24-hour forecasts were also quite similar. Differences were evident in the 12-hour forecasts where there was an increase in integrated moisture across southern Minnesota and western Iowa. Furthermore, there was a slightly moister regime in the WRFZ compared to the WRFX well preceding the moisture plume, over Michigan.

f. Error of experiment and control WRF 12-hour forecasts compared to GPS-IPW

The aforementioned case was representative of the mean quantitative results over the experiment period. Using GPS-IPW point observations, the 12-hour forecast comparison indicated that the WRFZ narrowly outperformed the WRFX with a lesser mean MAE for TPW by 0.05 mm. Table 6 compares the mean MAE and RMSE for the WRF simulations. For both the 24-hour and 36-hour forecasts, the WRFZ and WRFX performed statistically about the same, with a mean MAE difference no greater than 0.01 mm. During this period, the TPW MAE was lowest for the WRFZ 12-hour forecast nine of 21 times, or 43%. This was in comparison to the WRFX, which had the lowest MAE only five of 21 times, or 24%. The WRFY had the lowest MAE seven of 21 times, or 33%. WRF trends for MAE and RMSE over the experiment period are shown in Figure

11. This indicates that the WRFY analysis was competitive, but occasionally exhibited a higher MAE for individual misses than the WRFX and WRFZ, which increased its mean TPW MAE. Of particular interest is that the WRFY analyses exhibited a lower TPW MAE for four of the last five periods evaluated. The 12-hour forecast TPW MAE for the WRFY was likewise the lowest for four of the last five periods. This lends credence to the already seminal holding that NWP is an initial-value problem and more accurate ICs result in a more accurate forecast.

g. Error of experiment and control WRF 12-hour forecasts compared to NAM analysis

In order to confirm the result of the point comparison, a grid analysis comparison was arranged. The grid comparison used the NAM analysis of TPW, which contains the GPS-IPW observations as input. All grid points within the verification area were compared. The verification grid and forecast grid were collocated after re-projecting the verification analysis. This was completed through remapping and upscaling the NAM analysis from its native projection and resolution to that of the experiment domain. A bilinear interpolation was used as part of the subsampling. WRF model output was not re-projected. The mean TPW MAE calculated with this approach over the experiment period reached the same result as the GPS-IPW point-wise comparison. Using the NAM analysis and comparing all verification grid points, the WRFZ mean MAE was 0.04 mm less than the WRFX, which produced the next lowest mean MAE. Mean MAE and RMSE are compared in Table 7, and the trend throughout the evaluation period can be found in Figure 12. The WRFY exhibited the worst mean MAE, but that was only 0.16

mm greater than the WRFZ. The performance of the WRFX and WRFZ at the 24 and 36 hour forecasts were not discernible. Trends in MAE and RMSE are shown in Figure 13 for 24-hour forecasts and Figure 14 for 36-hour forecasts. Again, the difference in the mean MAE was 0.01 mm or less between the two for both forecast hours, as shown in Table 8 for 24-hour forecasts and Table 9 for 36-hour forecasts. The WRFY had a higher mean MAE at those forecast hours, but still indicated some strength relative to the WRFX and WRFZ during the last five periods.

h. Error of relative humidity forecasts compared to NAM analysis

In order to ascertain whether the GOES Sounder retrievals were able to improve low-level moisture analyses, mean MAE was calculated for relative humidity at 700 hPa and 850 hPa. A grid comparison to the NAM analysis was used for this inquiry. Radiosonde point observations were not used for this evaluation due to their limited coverage and, more importantly, because the Sippican Mark IIA GPS radiosondes in use at the NWS launch sites have been known to produce a dry bias and the moisture observations are “meteorologically inconsistent” with traditional understandings of a well-mixed boundary layer (VanCleve and Klimowski 2007). There is some evidence that the vertical distribution of moisture in NAM forecasts may also be erroneous due to limited correcting observations over the continental United States in analyses (R. Aune 2011, personal communication), but a disparate analysis is required. However, the differences between the mean MAE and RMSE, given in Table 10, were far too small to lead to any conclusive results. For example, examining 12-hour forecasts at 850 hPa, the mean MAE difference of relative humidity between the WRFX and WRFZ was 0.12%.

At 700 hPa for 12-hour forecasts, this difference was reduced to 0.02%. Trends in MAE over the experiment period are shown in Figure 15. In both cases, the WRFZ slightly outperformed the WRFX and WRFY. While these results are consistent with the mean TPW MAE results, additional observations or closer analysis would be required to determine if this difference is meaningful or significant for relative humidity.

A case from 00 UTC 10 November 2011 demonstrates the changes that the GOES Sounder assimilation process makes in producing the WRFZ analysis. The WRFZ was used because differences between the WRFZ analysis and the NAM analysis can be attributed solely to a single assimilation step. Figure 16 shows the TPW from the NAM analysis for the case, in which a strong mid-latitude weather system is exiting the eastern boundary of the grid. Figure 17 shows how the TPW analysis used to initialize the WRFX compared with the NAM. There is a dry bias over Lake Huron. In comparison to Figure 18, the TPW analysis for the WRFZ, the WRFX analysis contains less column-integrated moisture. The GOES-13 Sounder water vapor retrievals and cloud adjustments updated the analysis in the WRFZ to decrease bias in that area.

To determine whether the CRAS assimilation step adequately adjusted the atmospheric moisture profile in the correct location, 700 hPa and 850 hPa relative humidity values were compared to the NAM analysis. These levels were chosen because the cloudiness on the retreating side of the system was likely based in the lower troposphere. This was also consistent with the position of the “dry slot” advecting dry middle and upper tropospheric air into the system, which traditionally scours ice clouds. In addition, large differences in low-level relative humidity typically indicate meaningful

water vapor mixing ratio added to or subtracted from the profile. The 700 hPa relative humidity analysis from the NAM is shown in Figure 19. Compared to the WRFX analysis, it is evident that the WRFX exhibits a negative relative humidity bias at 700 hPa over Lake Huron, based on the difference shown in Figure 20. There was limited bias over the Ohio Valley. In comparison, the WRFZ analysis and comparison to the NAM analysis for this field, as shown in Figure 21, suggested the CRAS assimilation step produced a high bias over the Ohio Valley as the result of cloud assimilation. The CTP can have a high bias when there is an inversion in the reference profile (Schreiner et al. 2002). This manifests into greater moisture higher in the troposphere during the assimilation step. The dry bias over Lake Huron, where sky conditions were clear for water vapor retrievals, was less. In comparison, the 850 hPa relative humidity analysis from the NAM is shown in Figure 22. Figure 23 compares this analysis to the WRFX, which indicates a moist bias at 850 hPa along the Ohio River bordering Indiana, Ohio, and Kentucky. The impact of the Sounder assimilation is apparent in Figure 24, which depicts a much smaller bias in that location. The summary of this investigation is that the CRAS assimilation step was able to correct moisture in clear fields of view, and in some cloudy areas where the cloud assimilation used the correct CTP.

i. Impact on precipitation

Another synoptic-scale weather system traversing the continental United States provided a case, on 8 October 2011, in which the adjusted TPW resulted in a clearly advantageous precipitation forecast. Figure 25 shows TPW analyses for the WRFX and WRFZ on this morning. Morning TPW analyses from the WRFX valid 12 UTC 8

October 2011 indicate integrated moisture of up to 8 mm greater than the NAM analysis. The WRFZ analysis with the GOES Sounder retrieval input exhibited minimal bias in the moisture field, compared to the NAM analysis over this same area, as shown in Figure 26. The WRFZ TPW MAE computed based on the GPS-IPW observations was 1.58 mm, compared to 1.87 mm from the WRFX. This would have an impact on the quantity of the ensuing precipitation over the subsequent 12 hours. Figure 27 indicates that while the spatial coverage of precipitation between the WRFX and the WRFZ was very similar, the WRFZ produced less precipitation over south central Kansas. The WRFZ accumulated precipitation MAE computed based on the Stage II analysis was 1.48 mm, compared to 1.65 mm from the WRFX. Thus, the WRFZ amounts were more consistent with the multi-sensor NCEP Stage II precipitation analysis. The NCEP Stage II analysis is a multi-sensor product of accumulated precipitation which combines bias-corrected WSR-88D estimates with gage measurements. The advantage is leveraging the spatial patterns captured by radar with the truth amounts at limited locations within the radar coverage area. Though not without criticism, this product is more accurate than an analysis of one of its components, with most notable improvement during the spring and fall months when rainfall occurs on a larger spatial scale which aids in correlating gage measurements with radar returns (Seo 1998).

5. Cloud fraction results

The same effort has not been afforded to develop a cloud parameterization or verification analysis that serves both operational and modeling requirements. Adequate cloud representation has implications for NWP because clouds strongly control the radiation

budget in addition to their importance for transitions between water vapor, condensate, and precipitation. Furthermore, the NWS produces a forecaster-edited gridded sky cover forecast as part of the NDFD for their public forecast package. This forecast takes into account changes in cloud coverage over the celestial dome for an hour period. This has been challenging because NCEP operational model output of total sky cover does not meet this requirement. This has led to the development of heuristic approaches within NWS offices which are not well documented or tested. Consequently, NDFD verification for total sky cover has suffered (J. Craven 2010, personal communication).

a. WRF cloud fraction methodology

Xu and Randall (1996) developed the cloud fraction computation for the WRF based on the notion that grid-averaged condensate mixing ratio, consisting of cloud water and cloud ice, is a better diagnostic for stratiform cloudiness than grid-averaged relative humidity. The result is a coupling between the cloud fraction, $C_{fraction}$, condensate mixing ratio, and relative humidity, RH :

$$C_{fraction} = \begin{cases} RH^k [1 - \exp\left(\frac{-\beta_0 \bar{q}_l}{[(1 - RH)q_{vs}]^\tau}\right)], & \text{if } RH < 1 \\ 1, & \text{if } RH \geq 1 \end{cases}$$

where \bar{q}_l is the large-scale liquid water mixing ratio and q_{vs} is the saturation water vapor mixing ratio. The values of k , β_0 , and τ were determined empirically to be 0.25, 100, and 0.49, respectively. This formulation indicates that the cloud amount varies exponentially according to the grid-averaged condensate mixing ratio, which is the primary indicator of cloud fraction here. The rate of variation is a function of the grid-averaged relative humidity.

The cloud fraction is calculated at each point for each native model (sigma) level. The cloud fractions for vertical columns are combined based on a binning approach, where the final cloud fraction is assigned to a layer based on the greatest fraction for one level within the layer. The low, middle, and high layers are bounded by the surface, 642 hPa, 350 hPa, and 150 hPa. The final cloud fraction computed for each of these layers is the mean of the values within the vertical bounds.

The averaging of the three layers decreases the overall sky cover, which is not consistent with an observational perspective. For example, total coverage (100%) in the lowest level but clear skies above, a common scenario where stratiform cumulus may be expected, would lead to a WRF cloud fraction of only 33%. This is contrary to the working NWS definition which is forecast into the NDFD. Consequently, this experiment pursued results for verification of the total sky cover computed in the traditional way as well as in a maximum fraction method, where the final cloud fraction is calculated based on the maximum value from all three layers. Yet, this approach was still underdone because up to two cloud fractions were negated. For example, if there was widespread high cirrus above broken low clouds, the actual fraction from an observation perspective will be the sum of the lower cloud fraction and the product of the uncovered lower sky and the upper cloud fraction.

The WRF cloud fraction was compared to the NAM total sky cover analysis, as shown in Figure 28. This NAM analysis, also based on the Xu and Randall (1996) methodology, is typically a bimodal product (either clear or cloudy), though there are some gradients. The microphysical parameterization partitioning and controlling

interactions between species was primarily responsible for the magnitude of the cloud fraction. Furthermore, the computation of the NAM cloud fraction is not well documented. Thus, intricacies in the calculation may evade analysis. However, because cloud fraction is a component of the model's radiation budget, the calculated function is not anticipated to be unreasonable from a large-scale perspective. The Xu and Randall (1996) methodology was originally formulated for climate models, which traditionally have a larger spacing of grid points.

b. Motivation for CRAS cloud fraction

The cloud fraction computation in the CRAS was motivated to improve the sky cover composites in the NDFD. The NDFD sky grid, which is adjusted by a human forecaster at each of the NWS offices across the country for a small subset that is the forecaster's local area of responsibility (AOR), have diminished integrity as the result of fractional discontinuities between AORs, as well as limited gradients within AORs. Existing operational NWP models do not provide a sufficient first-guess for sky cover. Relative humidity has traditionally been a substantial portion of the cloud formulation.

The NWS definition for sky cover is "the expected amount of opaque clouds (in percent) covering the sky valid for the indicated hour" (National Weather Service 2011). There is no probabilistic component and no definition of "opaque cloud" or "cloud" (J. Craven 2010, personal communication). The implication is that the sky cover product represents cloud coverage of the celestial dome (all sky visible from an all-seeing point observer). There is not an outright radiative component of the sky cover formulation adopted by the NWS. Thus, the CRAS cloud fraction is not used and was not intended

for radiative balances in the model; it is derived as part of the post-processing, parameter calculations. It is a “partly cloudy” scheme which does not rely on relative humidity.

c. CRAS cloud fraction methodology

The methodology for the CRAS cloud concentration is based out of the fairly loose constraints set forth by the NWS and is thus fairly ad hoc and founded on simple physical principles. To summarize this approach, for each model grid point, a cloud concentration profile is calculated. The average profile for the upper and lower troposphere is based on the number of cloud layers, which determine the local sky cover. Adjacent grid points are combined with the central grid point to form an upper and lower celestial dome, with preference given to the lower celestial dome, since it is closer to the theoretical observer and could obscure the upper dome.

In articulating the method, the first step is to compute a point-by-point, level-by-level cloud concentration. For every grid point at each vertical level, if the cloud mixing ratio is greater than or equal to 0.01 g/kg, a ratio is computed between this mixing ratio and the auto-conversion limit (based solely on the temperature at that grid point). The resulting ratio, generally between zero and one, is the fraction of cloud water to the maximum cloud water possible at a point without a precipitation process. Thus, a ratio greater than one implies that the cloud at that point, on that level, is precipitating.

The cloud-to-precipitation auto-conversion limit, *ACL*, is a piecewise function which returns the maximum non-precipitating cloud mixing ratio in g/g. The *ACL* is greatest and constant for warm clouds, which are greater than freezing, and thus in liquid phase. As shown in Figure 29, the slope of *ACL* is steepest at 261 K, the temperature at

which there is maximum ice growth, and the typical average temperature when cloud transitions from liquid to ice:

$$T \geq 273: ACL = 0.001$$

$$261 \leq T < 273: ACL = 0.001 - 0.005 \left(\frac{273 - T}{12} \right)^3$$

$$249 \leq T < 261: ACL = 0.0001 + 0.004 \left(\frac{T - 249}{12} \right)^3$$

$$T < 249: ACL = 0.0001$$

Essentially, the fraction of mixing ratio to ACL is a first guess at how much each test point is attenuating shortwave radiation due to cloud. If the sigma level of the test point is greater than 0.5 (approximately 500 hPa), then the ratio is half of the original value. This ad hoc approach prevents ice cloud, which is typically thin and reflective, from producing overcast conditions. Since the upper half of the troposphere is largely cold and dry, the fraction of mixing ratio to ACL is not an ideal approximation. The next step is to vertically average the ratios at each grid point. One average is done for all test points at or above $\sigma = 0.5$, another is done for those below.

If any of the layers averaged below $\sigma = 0.5$ have a cloud mixing ratio greater than the ACL , then the cloud cover ratio is set to one (100%). Overcast conditions are assumed at grid points where precipitation is occurring. For the layers averaged at or above $\sigma = 0.5$, if the vertical average is greater than 0.5 (50%), then the cloud cover is lowered to 0.5 (for the upper troposphere component) because ice cloud is rarely observed to attenuate light like water cloud (S. Hentz 2009, personal communication). The following step is to combine the two ratio averages into a sky cover.

To create the upper celestial dome for ice cloud at every grid point, the ratio average for each adjacent grid point contributes to 20% of the total. The final 20% contribution comes from the vertical ratio average of the grid point itself. To create the lower celestial dome for water cloud for every grid point, the vertical ratio average for each adjacent grid point contributes to 10% of the total. The final 60% contribution comes from the vertical ratio average of the grid point itself. This approach was implemented because the upper celestial dome is spatially larger to the observer than the lower celestial dome, if not obscured.

Finally, to produce sky cover output, SC , in percent covered at each vertical column in the model horizontal domain, the result from the lower celestial dome, LCD , computation is added to the upper celestial dome, UCD , computation over the lower dome area left uncovered by the water cloud. Upper cloud will not contribute to a sky cover fraction if it is obstructed by lower cloud. Thus, $SC = LCD + (1-LCD)(UCD)$. If the resulting sky cover is less than 5%, SC is readjusted to 0% due to the limited predictability of small coverage amounts.

d. Results

To assess the benefit of the CRAS algorithm, the mean sky cover MAE was computed during the experiment period and compared with the default WRF sky cover algorithm output as well as the recomputed maximum fraction. The truth used to compute the mean MAE for each comparison was taken from the NDFD one-hour forecast and NAM analysis. The trend of sky cover MAE for the WRF runs, based on the default calculation, and CRAS over the experiment period is shown in Figure 30.

Corresponding plots for the trend in MAE for the WRF runs using the maximum fraction calculation are found in Figure 31. While the skill of the CRAS dynamics and physics, which provide the input atmosphere for the sky cover algorithm, was thought to underperform based on the generally poor performance of the WRFY in TPW and related verification, the algorithm was built to fit the CRAS and not easily applied to the WRF model. Figure 32 shows the NDFD one-hour forecast compared to the CRAS as well as the default and maximum methods of the WRFX sky cover calculation. It shows the superior performance of the CRAS algorithm from increased cloudiness over Wisconsin and northern Michigan matching the pattern of the NDFD one-hour forecast grid. The WRFX has very little cloud cover in that corridor.

With the NDFD one-hour forecast used as truth, the CRAS 12-hour forecast resulted in a mean sky cover MAE of 14.76% compared to between 17.97% and 18.84% for the WRF control and experimental runs' corresponding forecast using the maximum fraction computation, as shown in the second data row of Table 11, and between 20.39% and 20.87% for the WRF control and experiment runs' corresponding forecast using the default calculation, as shown in the second data row of Table 12. This mean MAE was the lowest of all model runs for all forecast times against each analysis. The result was anticipated because the development of the CRAS algorithm was guided by a need for the numerical representation of model output in an observable sky field. With the NAM analysis used as truth, the CRAS 12-hour forecast resulted in a mean sky cover MAE of 29.68% compared to between 30.04% and 31.00% for the WRF control and experimental runs' corresponding forecast using the maximum fraction computation, as shown in the first data row of Table 11, and between 32.43% and 32.86% for the WRF control and

experimental runs' corresponding forecast using the default calculation, as shown in the first data row of Table 12. Differences between the WRF control and experimental runs were not substantial in either case. That is, the deficiencies in the total sky cover output and lack of a suitable validating analysis overshadowed any impact of the GOES Sounder cloud assimilation.

The performance of the CRAS algorithm, though, was noteworthy, especially in cases where cloudiness was observed across a large extent of the domain. The result was observed in the comparisons involving the calculation of mean sky cover MAE using the maximum fraction re-calculation as well as the traditional, layer-averaged approach. In cloudy cases, the maximum fraction approach produced a greater sky cover and thus was more competitive with the CRAS.

The other interesting element was that the mean sky cover MAE for the CRAS did not substantially increase between the 12-hour forecast and 36-hour forecast. For example, the mean sky cover MAE when computed using the NAM analysis as truth only increased from 29.68% at the 12-hour forecast to 30.62% at the 36-hour forecasts. Similar small increases of mean sky cover MAE with forecast hour were also found for the WRF control and experimental runs. Even the mean sky cover MAE from the CRAS at its best, using the NDFD one-hour forecast, was not particularly good, considering that for an oversimplified bimodal case in which all grid points were either clear or cloudy, a MAE of 15% is equivalent to a misclassification over 600,000 km², which is slightly smaller than the combined surface area of North Dakota, South Dakota, and Minnesota. To extend this analogy, if cloud coverage associated with a middle-latitude weather

system was simplified and represented by an overcast fraction across its length scale, a synoptic system would need to be misplaced on the model grid by approximately 400 km, the approximate distance from Fargo, North Dakota, to Duluth, Minnesota, at some point over the 36-hour simulation to produce a sky cover MAE that substantial. The other verified fields, such as PW, suggest that this was not the case. All of the cloud fraction algorithms, or the analyses they were verified against, were too imprecise to produce any meaningful results based on the predictability of synoptic features within the model domain. Given this, finding skill in mesoscale enhancements to the analysis cloud field is unlikely and not recognized in this study.

6. Conclusions

This study was an initial investigation into the benefits of using GOES-13 Sounder retrievals as part of regional NWP to improve forecasts of TPW, sky cover, relative humidity, and precipitation. In the evaluations conducted here, the retrievals were found to be inconsequential in many cases and did not produce a consistent positive reflection in the statistics. This indicates that instruments onboard our earth-observing geostationary satellites need spectral improvement to supply a meaningful correction to analyses used in regional NWP. It also requires a reassessment of how the operational NWP community uses indirect moisture information from remote sources beyond the techniques explored here. While the results presented are perhaps a testament to the adequacy of current analyses, they stand as a challenge to improve numerical techniques for assimilating additional data because the number of data sets assimilated into operational models continues to grow. Yet, NWP solutions are far from perfect and, as

demonstrated, there is information from the GOES Sounder which can improve moisture representation in models and alter forecasts for the better.

Benefits were expected in part due to a casting of the ARW governing equations in flux form in conjunction with the KF convective parameterization, which is sensitive to variations in middle and upper tropospheric relative humidity as part of its formulation. The method and results were tempered based on the limited vertical resolution of the GOES Sounder. During the summer months, the GOES Sounder water vapor channels are most capable of detecting temperature and moisture gradients in the upper troposphere, and sense relatively little, if any, boundary layer moisture. A one-dimensional variational assimilation scheme was used to add or subtract water vapor from a model sounding, indiscriminately of vertical gradients, based on three sigma-bounded layers produced by the Li et al. (2008) enhancements to the retrieval process.

Comparing WRFX and WRFZ, two sources of PW verification confirmed forecasts were slightly better 12 hours after initialization if GOES-13 Sounder input was included. Results were calculated based on the GPS-IPW network and confirmed using a NAM analysis. A few case studies indicated the potential for better precipitation forecasts when compared with the NCEP Stage II analysis. However, the dexterity of the model analyses produced from the CRAS was far from certain. Even greater uncertainty is presumed to exist for analyses at higher spatial resolutions and model simulations with explicit convection. Cloud cover assimilation resulted in additional moisture occasionally placed too high in the column and retrievals did not always positively influence the analysis and forecast. There was no substantial impact of the added

observations at 24 or 36 hours in the flow regime of the period studied from late September into early October. While the WRFY had fleeting success, the indications were that the CRAS dynamics and physics were controlling and negatively influencing the solution, even at short intervals from the initialization time. Despite this, the CRAS sky cover algorithm showed improvement compared to legacy NWP formulations, including the current WRF cloud fraction method, which led to undesirable cloud cover results for the control and experimental runs in this study.

Thus, in order for an accurate forecast of cloud, water vapor, and precipitation distributions, it is necessary for our NWP models to contain a detailed and accurate analysis of moisture. The current NCEP operational models are good, but there remains a small margin for improvement from assimilating additional observations if done so with skill and knowledge of the dynamics and parameterizations within the model that would respond to such changes in producing a forecast. At the current time, this is only possible through the use of satellite products. Using the CRAS pre-forecast and assimilation techniques in conjunction with the WRF has allowed for GOES Sounder observations in the form of retrievals to impact the solution. The WRF transition experiment conducted during the early fall of 2011 has been able to better quantify the degree of this effect, and will continue in real-time for upcoming seasons. While the results are tempered by some inherent shortcomings in the capabilities of the instrument, assimilation scheme, and numerical model, the strategy and path forward are clear. A delicate investigation of moisture integration techniques within assimilation constraints and model parameterizations for different seasons and flow regimes can slowly extract gainful information from the current, and future, geostationary platforms.

References

- Askne, J., and H. Nordius, 1987: Estimation of tropospheric delay for microwaves from surface weather data. *Radio Sci.*, **22**, 379–386.
- Aune, R. M., 1994: Improved precipitation predictions using total precipitable water from VAS. Preprints, *10th Conference on Numerical Weather Prediction*, American Meteorological Society, Portland, OR, 192–194.
- Aune, R. M., 1996: Initializing cloud predictions using the GOES-8 sounder. Preprints, *8th Conference on Satellite Meteorology and Oceanography*, American Meteorological Society, Atlanta, GA.
- Baldwin, M. E., J. S. Kain, and M. P. Kay, 2002: Properties of the convection scheme in NCEP's Eta Model that affect forecast sounding interpretation. *Wea. Forecasting*, **17**, 1063–1079.
- Bayler, G., R. M. Aune and W. H. Raymond, 2000: NWP cloud initialization using GOES sounder data and improved modeling of nonprecipitating clouds. *Mon. Wea. Rev.*, **128**, 3911–3920.
- Duan, J., and Coauthors, 1996: GPS meteorology: direct estimation of the absolute value of precipitable water. *J. Appl. Meteor.*, **35**, 830–838.
- Dudhia, J., 1989: Numerical study of convection observed during the winter monsoon experiment using a mesoscale, two-dimensional model. *J. Atmos. Sci.*, **46**, 3077–3107.

- Filiberti, M. A., L. Eymard, and B. Urban, 1994: Assimilation of satellite precipitable water in a meteorological forecast model. *Mon. Wea. Rev.*, **122**, 486–506.
- Gal-Chen, T., B. D. Schmidt, and L. W. Uccellini, 1986: Simulation experiments for testing the assimilation of geostationary satellite temperature retrievals into a numerical prediction model. *Mon. Wea. Rev.*, **114**, 1213–1230.
- Gunshor, M., Cooperative Institute for Meteorological Satellite Studies, Space Science and Engineering Center, cited 2011: CIMSS GOES Weighting Functions. [Available online at <http://cimss.ssec.wisc.edu/goes/wf/>.]
- Gutman, S. I., S. R. Sahn, S. G. Benjamin, B. E. Schwartz, K. L. Holub, J. Q. Stewart, and T. L. Smith, 2004: Rapid retrieval and assimilation of ground based GPS precipitable water observations at the NOAA Forecast Systems Laboratory: Impact on weather forecasts. *J. Meteor. Soc. Japan*, **82**, 351–360.
- Haines, S. L., G. J. Jedlovec, and S. M. Lazarus, 2007: A MODIS sea surface temperature composite for regional applications. *IEEE Trans. Geosci. Remote Sens.*, **45**, 2919–2927.
- Hayden, C. M. and R. J. Purser, 1995: Recursive filter objective analysis of meteorological fields; Applications to NESDIS operational processing. *J. Appl Meteor.*, **34**, 3–15.
- Heymsfield, A. J., and L. J. Donner, 1990: A scheme for parameterizing ice cloud water content in general circulation models. *J. Atmos. Sci.*, **47**, 1865–1877.
- Kain, J. S. and J. M. Fritsch, 1990: A one-dimensional entraining/detraining plume model and its application in convective parameterization. *J. Atmos. Sci.*, **47**, 2784–2802.

- Kain, J. S., 2004: The Kain–Fritsch convective parameterization: an update. *J. Appl. Meteor.*, **43**, 170–181.
- Keyser, D., Environmental Modeling Center, National Weather Service, cited 2011: PREPBUFR Processing at NCEP. [Available online at http://www.emc.ncep.noaa.gov/mmb/data_processing/prepbuftr.doc/document.htm.]
- Knupp, K. R. and W. R. Cotton, 1985: Convective cloud downdraft structure: an interpretive survey. *Rev. Geophys.*, **23**, 183–215.
- Kuo, Y. H., Y. R. Guo, and E. R. Westwater, 1993: Assimilation of precipitable water measurements into a mesoscale numerical model. *Mon. Wea. Rev.*, **121**, 1215–1238.
- Lee, I. Y., 1992: Comparison of cloud microphysics parameterizations for simulation of mesoscale clouds and precipitation. *Atmos. Environ.*, **26A**, 2699–2712.
- Leslie, L. M., L. W. Logan, D. J. Gauntlett, G. A. Kelly, J. L. McGregor, and M. J. Manton, 1985: A high resolution primitive equation NWP model for operations and research. *Aust. Meteo. Mag.*, **33**, 11–35.
- Li, Jun, Jinlong Li, J. Otkin, T. J. Schmit, C.-Y. Liu, 2011: Warning Information in a preconvection environment from the geostationary Advanced Infrared Sounding System—a simulation study using the IHOP case. *J. Appl. Meteor. Climatol.*, **50**, 776–783.

- Li, Z., J. Li, W. P. Menzel, T. J. Schmit, J. P. Nelson, III, J. Daniels, and S. A. Ackerman, 2008: GOES sounding improvement and applications to severe storm nowcasting, *Geophys. Res. Lett.*, **35**, L03806.
- Ma, X. L., T. J. Schmit, and W. L. Smith, 1999: A nonlinear physical retrieval algorithm—Its application to the GOES-8/9 sounder, *J. Appl. Meteorol.*, **38**, 501–513.
- Market, P., S. Allen, R. Scofield, R. Kuligowski, and A. Gruber, 2003: Precipitation efficiency of warm-season Midwestern mesoscale convective systems. *Wea. Forecasting*, **18**, 1273–1285.
- McGregor, J. L., L. M. Leslie and D. J. Gauntlett, 1978: The ANMRC limited area model: Consolidated formulation and operational results. *Mon. Wea. Rev.*, **106**, 427–438.
- National Weather Service, cited 2011: National Digital Forecast Database. [Available online at <http://www.nws.noaa.gov/ndfd/definitions.htm>.]
- Raymond, W. H., 1988: High-order low-pass implicit tangent filters for use in finite area calculations. *Mon. Wea. Rev.*, **116**, 2132–2141.
- Raymond, W. H., W. S. Olsen, and G. Callan, 1995: Diabatic forcing and initialization with assimilation of cloud and rainwater in a forecast model. *Mon. Wea. Rev.*, **123**, 366–382.
- Raymond, W. H., and R. M. Aune, 1998: Improved precipitation forecasts using parameterized feedbacks in a hydrostatic forecast model. *Mon. Wea. Rev.*, **126**, 693–710.

- Raymond, W. H., and R. M. Aune, 2003: Conservation of moisture in a Kuo-type cumulus parameterization. *Mon. Wea. Rev.*, **131**, 771–779.
- Schmit, T. J., J. Li, J. J. Gurka, M. D. Goldberg, K. Schrab, J. Li, and W. Feltz, 2008: The GOES-R ABI (Advanced Baseline Imager) and the continuation of current sounder products. *J. Appl. Meteor.*, **47**, 2696–2711.
- Schreiner, A. J., T. J. Schmit, and R. M. Aune, 2002: Maritime inversions and the GOES sounder cloud product. *Nat. Wea. Dig.*, **26**, 27–38.
- Seo, D. J., 1998: Real-time estimation of rainfall fields using radar rainfall and rain gauge data. *J. of Hydrol.*, **208**, 37–52.
- Shepherd, J. M., B. S. Ferrier, P. S. Ray, 2001: Rainfall morphology in Florida convergence zones: a numerical study. *Mon. Wea. Rev.*, **129**, 177–197.
- Skamarock, W. C., J. B. Klemp, J. Dudhia, D. O. Gill, D. M. Barker, W. Wang and J. G. Powers, 2008: A description of the Advanced Research WRF version 3. *NCAR Technical Note*, **TN-468+STR**, 113 pp.
- Skamarock, W. C., M. L. Weisman, 2009: The impact of positive-definite moisture transport on NWP precipitation forecasts. *Mon. Wea. Rev.*, **137**, 488–494.
- Smith, W. L., 1966: Note on the relationship between total precipitable water and surface dew point. *J. Appl. Meteor.*, **5**, 726–727.
- Sundqvist, H., E. Berge, and J. E. Kristjansson, 1989: Condensation and cloud parameterization studies with a mesoscale numerical weather prediction model. *Mon. Wea. Rev.*, **117**, 1641–1659.

Tompkins, A. M., 2001: Organization of tropical convection in low vertical wind shears: the role of water vapor. *J. Atmos. Sci.*, **58**, 529–545.

VanCleve, D., and B. A. Klimowski, 2007: Addressing the Sippican Mark IIA Radiosonde Dry Bias at the NOAA/NWS Weather Forecast Office in Flagstaff, AZ. Abstracts, *32nd Annual Meeting*, Reno, NV, Nat. Weather Association, 7.5.

Xu, K.-M., and D. A. Randall, 1996: A semiempirical cloudiness parameterization for use in climate models. *J. Atmos. Sci.*, **53**, 3084–3102.

Tables

Dynamics	Non-Hydrostatic
Cumulus Scheme	Kain-Fritsch
Microphysics Scheme	WSM Single-Moment 5-Class
PBL Scheme	Yonsei University
Land Surface Scheme	NOAH
Surface Layer Physics	Monin-Obukhov with heat and moisture surface fluxes
Long Wave Radiation	RRTM
Short Wave Radiation	Dudhia Scheme
Time-Integration Scheme	Runge-Kutta 3 rd Order
Damping	Rayleigh

TABLE 1. The core configuration for the Weather Research and Forecasting (WRF) model used in the experiment. The dynamical package was the Advanced Research WRF (ARW). Each simulation had an adaptive time step. References for the schemes can be found in the Skamarock et al. (2008) technical note.

GPS-IPW	NAM-00	RUC-00	GFS-00
MAE	1.04	1.24	1.43
RMSE	1.41	1.65	1.87

TABLE 2. Mean values of mean absolute error (MAE) and root-mean-square error (RMSE) of total precipitable water (mm) over the period from 00 UTC 28 September 2011 to 00 UTC 8 October 2011. Error is calculated based on the GPS-IPW network as truth compared to the analyses of the NAM, RUC, and GFS.

GPS-IPW	WRFX-00	WRFY-00	WRFZ-00
MAE	1.58	1.61	1.59
RMSE	2.07	2.11	2.10

TABLE 3. Mean values of mean absolute error (MAE) and root-mean-square error (RMSE) of total precipitable water (mm) over the period from 00 UTC 28 September 2011 to 00 UTC 8 October 2011. Error is calculated based on the GPS-IPW network as truth compared to the analyses of the WRFX, WRFY, and WRFZ.

Sounder	WRFX-00	WRFY-00	WRFZ-00
MAE	1.61	1.60	1.44
RMSE	2.13	2.11	1.92

TABLE 4. Mean values of mean absolute error (MAE) and root-mean-square error (RMSE) of total precipitable water (mm) over the period from 00 UTC 28 September 2011 to 00 UTC 8 October 2011. Error is calculated based on the GOES-13 Sounder Ma retrievals as truth compared to the analyses of the WRFX, WRFY, and WRFZ.

Sounder	NAM-00	RUC-00	GFS-00
MAE	1.76	2.13	1.69
RMSE	2.38	2.81	2.23

TABLE 5. Mean values of mean absolute error (MAE) and root-mean-square error (RMSE) of total precipitable water (mm) over the period from 00 UTC 28 September 2011 to 00 UTC 8 October 2011. Error is calculated based on the GOES-13 Sounder Ma retrievals as truth compared to the analyses of the NAM, RUC, and GFS.

GPS-IPW	WRFX-12	WRFY-12	WRFZ-12
MAE	1.77	1.81	1.72
RMSE	2.27	2.37	2.24

TABLE 6. Mean values of mean absolute error (MAE) and root-mean-square error (RMSE) of total precipitable water (mm) over the period from 00 UTC 28 September 2011 to 00 UTC 8 October 2011. Error is calculated based on the GPS-IPW network as truth compared to the 12-hour forecasts of the WRFX, WRFY, and WRFZ.

NAM	WRFX-12	WRFY-12	WRFZ-12
MAE	1.97	2.09	1.93
RMSE	2.59	2.78	2.56

TABLE 7. Mean values of mean absolute error (MAE) and root-mean-square error (RMSE) of total precipitable water (mm) over the period from 00 UTC 28 September 2011 to 00 UTC 8 October 2011. Error is calculated based on the NAM analysis as truth compared to the 12-hour forecasts of the WRFX, WRFY, and WRFZ.

NAM	WRFX-24	WRFY-24	WRFZ-24
MAE	2.17	2.32	2.16
RMSE	2.84	3.07	2.83

TABLE 8. Mean values of mean absolute error (MAE) and root-mean-square error (RMSE) of total precipitable water (mm) over the period from 00 UTC 28 September 2011 to 00 UTC 8 October 2011. Error is calculated based on the NAM analysis as truth compared to the 24-hour forecasts of the WRFX, WRFY, and WRFZ.

NAM	WRFX-36	WRFY-36	WRFZ-36
MAE	2.43	2.71	2.42
RMSE	3.18	3.57	3.18

TABLE 9. Mean values of mean absolute error (MAE) and root-mean-square error (RMSE) of total precipitable water (mm) over the period from 00 UTC 28 September 2011 to 00 UTC 8 October 2011. Error is calculated based on the NAM analysis as truth compared to the 36-hour forecasts of the WRFX, WRFY, and WRFZ.

NAM	WRFX-12	WRFY-12	WRFZ-12
700 hPa	9.26	10.42	9.24
850 hPa	9.47	9.90	9.35

TABLE 10. Mean values of mean absolute error (MAE) of relative humidity (%) at 700 hPa and 850 hPa over the period from 00 UTC 28 September 2011 to 00 UTC 8 October 2011. Error is calculated based on the NAM analysis as truth compared to the 12-hour forecasts of the WRFX, WRFY, and WRFZ.

MAE	WRFX-12	WRFY-12	WRFZ-12	CRAS-12
NAM	29.95	31.00	30.06	29.68
NDFD	17.97	18.84	18.11	14.76

TABLE 11. Mean values of mean absolute error (MAE) of total sky cover (%) over the period from 00 UTC 28 September 2011 to 00 UTC 8 October 2011. Error is calculated based on the NAM analysis and NDFD one-hour forecast as truth compared to the 12-hour forecasts of the WRFX, WRFY, WRFZ, and CRAS. The WRF sky cover was calculated using the layer with the highest fraction for each grid point.

MAE	WRFX-12	WRFY-12	WRFZ-12	CRAS-12
NAM	32.43	32.86	32.50	29.68
NDFD	20.39	20.87	20.51	14.76

TABLE 12. Mean values of mean absolute error (MAE) of total sky cover (%) over the period from 00 UTC 28 September 2011 to 00 UTC 8 October 2011. Error is calculated based on the NAM analysis and NDFD one-hour forecast as truth compared to the 12-hour forecasts of the WRFX, WRFY, WRFZ, and CRAS. The WRF sky cover was calculated using the default algorithm.

Figures

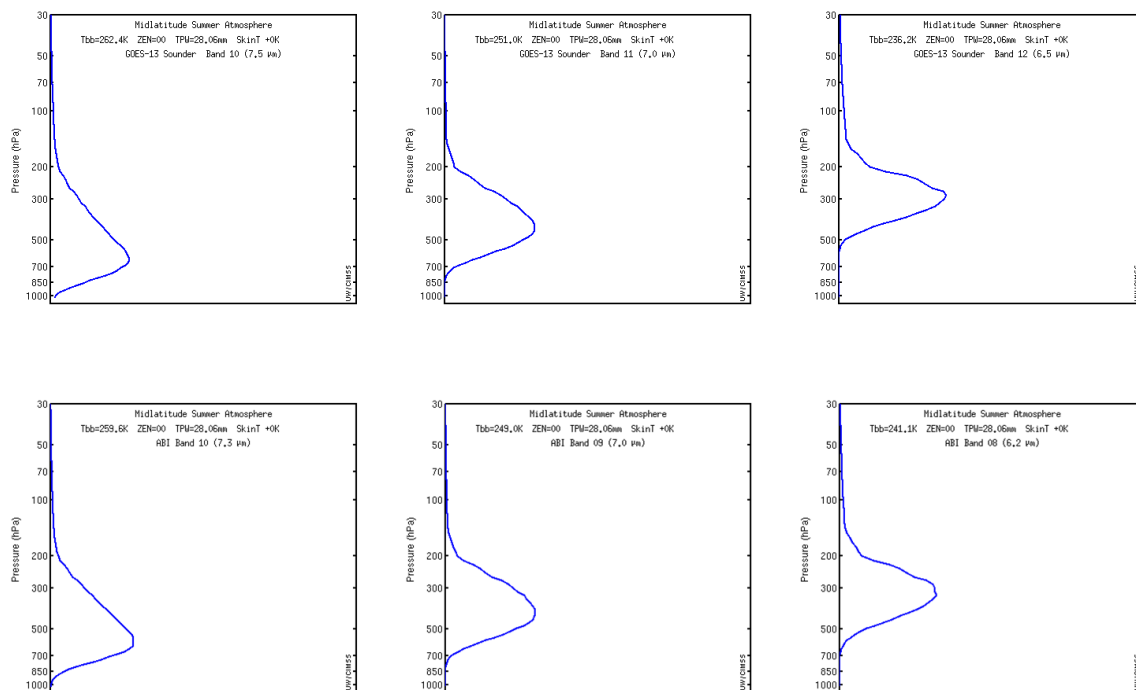


FIG. 1. Water vapor weighting functions for the GOES-13 Sounder (top) and future GOES-R ABI (bottom) in an idealized mid-latitude summer atmosphere sounding observed at a zero-degree zenith angle (Gunshor et al. 2011). The total precipitable water is 28.06 mm. For the GOES-13 Sounder, the central wavelengths are 7.5 μm , 7.0 μm , and 6.5 μm (left to right). For the GOES-R ABI, the central wavelengths are 7.3 μm , 7.0 μm , and 6.2 μm (left to right). Their observation capabilities are similar. Water vapor weighting functions are a function of both temperature and moisture content. The strength of the GOES-13 Sounder and GOES-R ABI is sensing middle tropospheric water vapor.

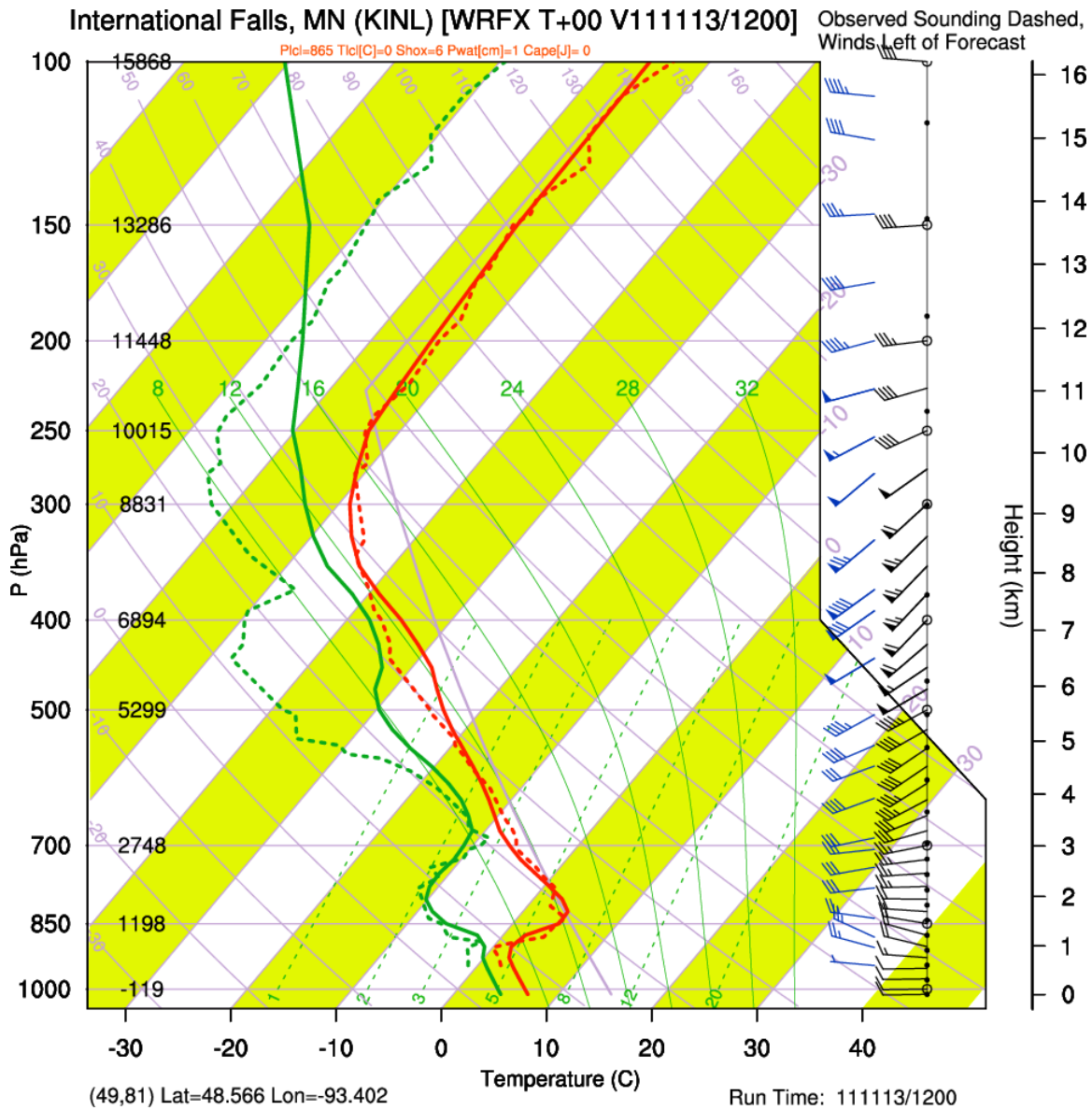


FIG. 2. A skew-T log-P diagram comparing the observed sounding from a radiosonde launched from International Falls, Minnesota, at 12 UTC on 13 November 2011 (dashed) with the background sounding (solid) used at the nearest grid point in the re-projected GFS analysis valid at the same time. Visibly substantial differences to the dew point profile above the tropopause are quantitatively very small in mixing ratio. Temperature is in red; dew point is in green.

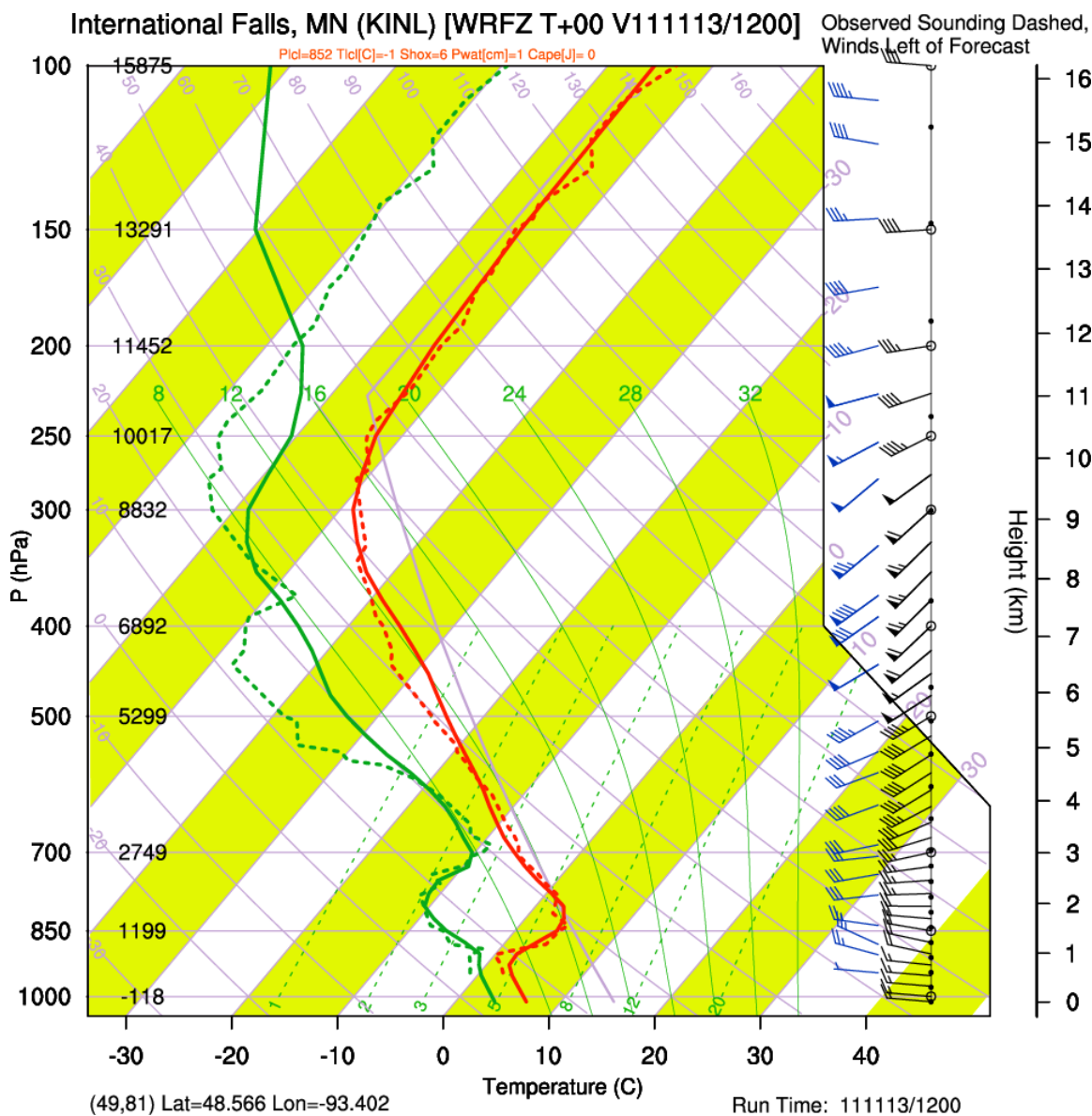


FIG. 3. A skew-T log-P diagram comparing the observed sounding from a radiosonde launched from International Falls, Minnesota, at 12 UTC on 13 November 2011 (dashed) with a sounding from the re-projected GFS analysis valid at the same time adjusted with a water vapor retrieval. The background sounding is from the nearest point of the GFS analysis grid with a correction based on water vapor retrieval assimilation in the CRAS. Temperature is in red; dew point is in green.

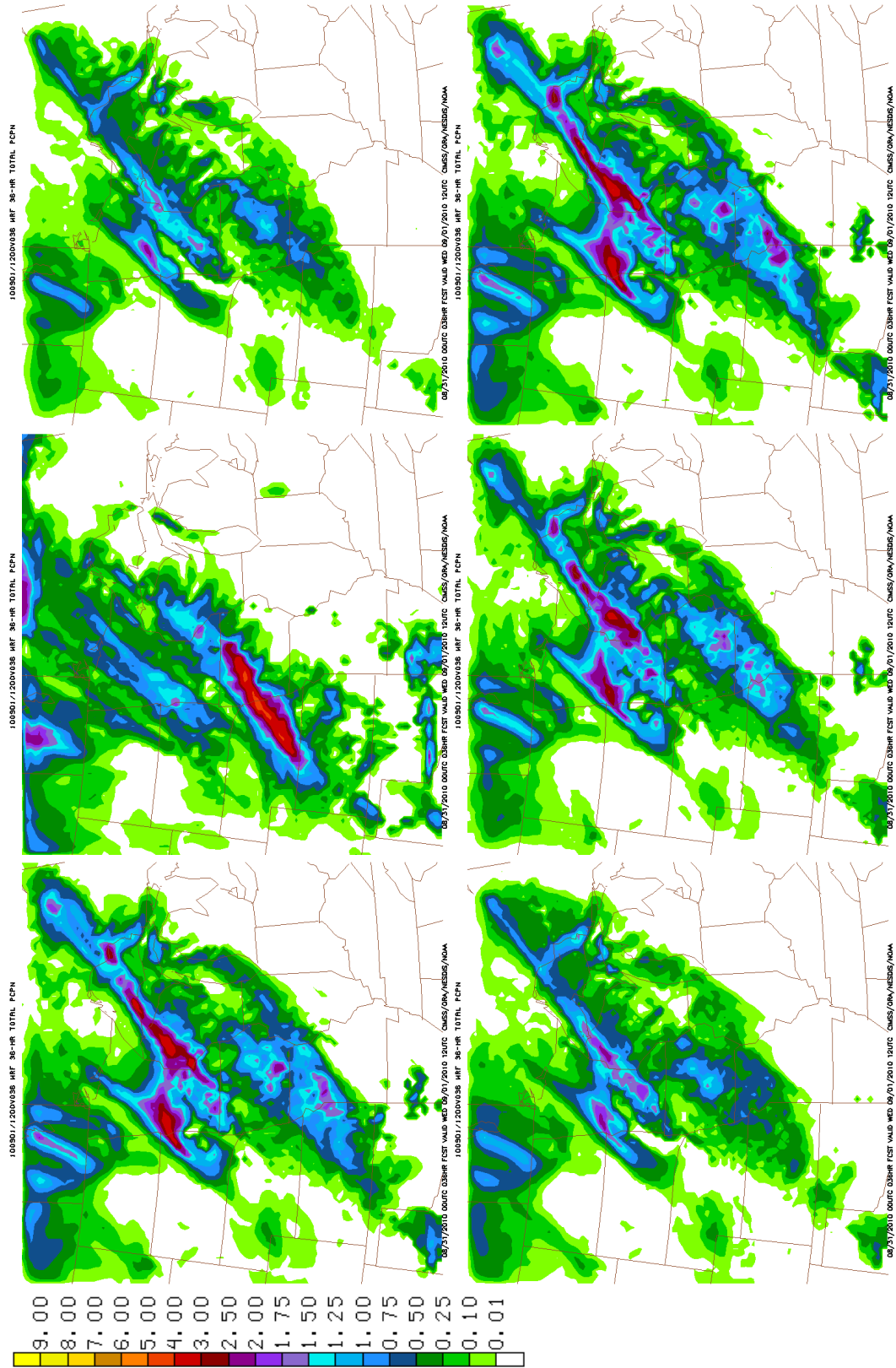


FIG. 4. The 36-hour accumulated precipitation ending 12 UTC 1 September 2010 from various WRF runs initialized at 00 UTC 31 August 2010. From upper-left to lower-right horizontally, these runs contain initial and boundary conditions consisting of: operational GFS output, CRAS output containing satellite observations in the pre-forecast procedure, GFS output with 90% of the original relative humidity (RH), GFS output with 90% of the original RH between the surface and 800 hPa, GFS output with 90% of the original RH between 750 hPa and 400 hPa, and GFS output with 90% of the original RH between 350 hPa and 100 hPa.

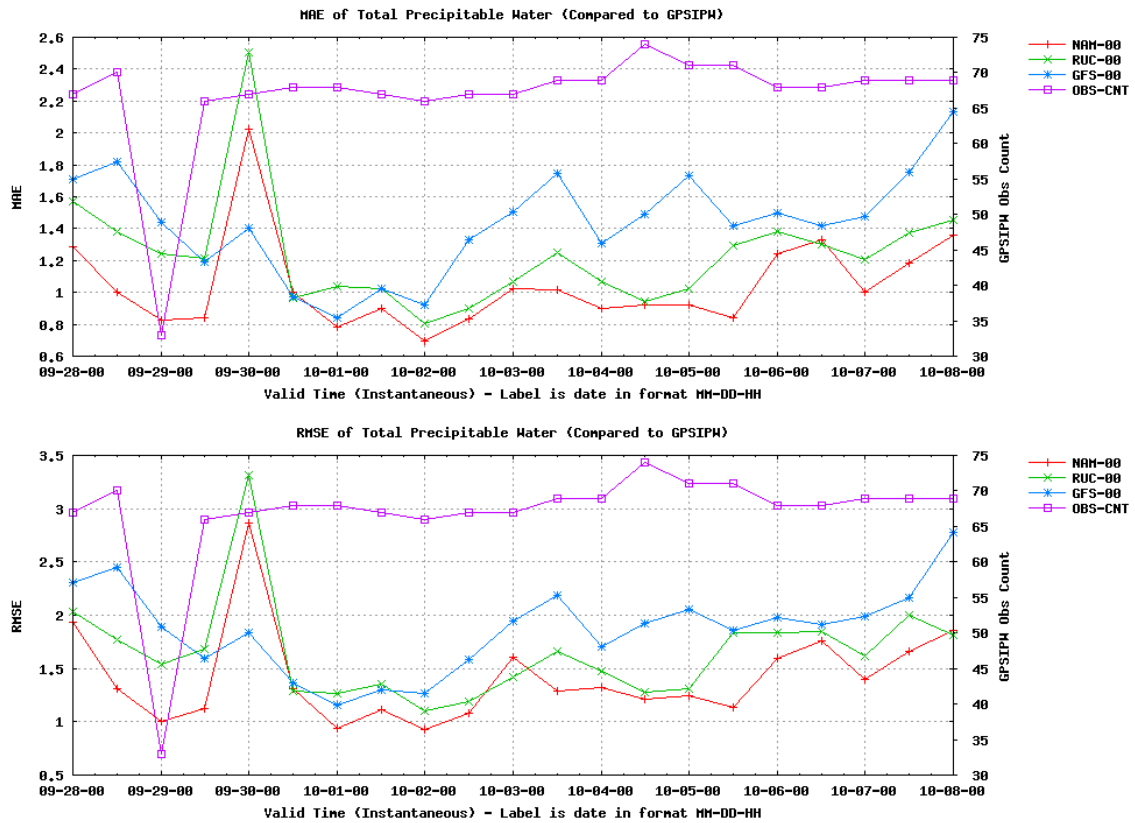


FIG. 5. Mean absolute error (top) and root-mean-square error (bottom) for total precipitable water (mm) over the period from 00 UTC 28 September 2011 to 00 UTC 8 October 2011. Error is calculated based on the GPS-IPW network at the valid time compared to the analyses of the NAM (red), RUC (green), and GFS (blue) for the same time. The observation count (purple) is plotted on the right ordinate axis.

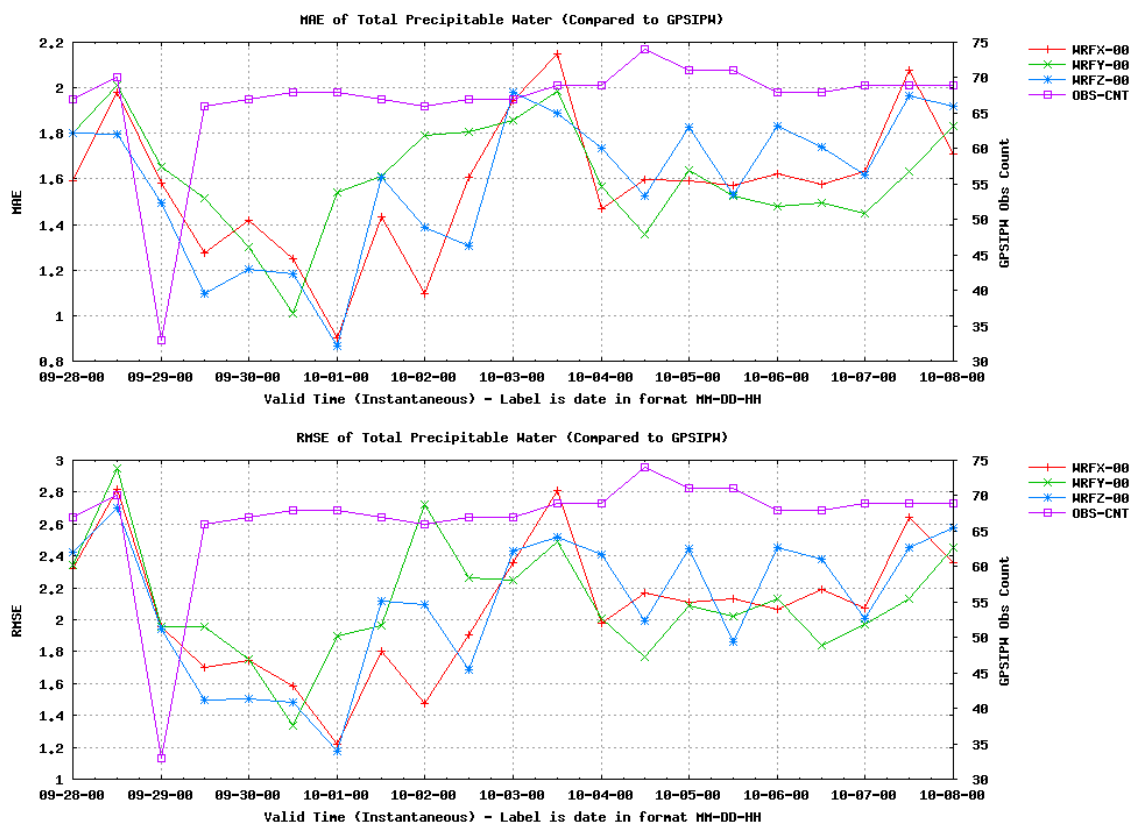


FIG. 6. Mean absolute error (top) and root-mean-square error (bottom) for total precipitable water (mm) over the period from 00 UTC 28 September 2011 to 00 UTC 8 October 2011. Error is calculated based on the GPS-IPW network at the valid time compared to the analyses of the WRFX (red), WRFY (green), and WRFZ (blue) for the same time. The observation count (purple) is plotted on the right ordinate axis.

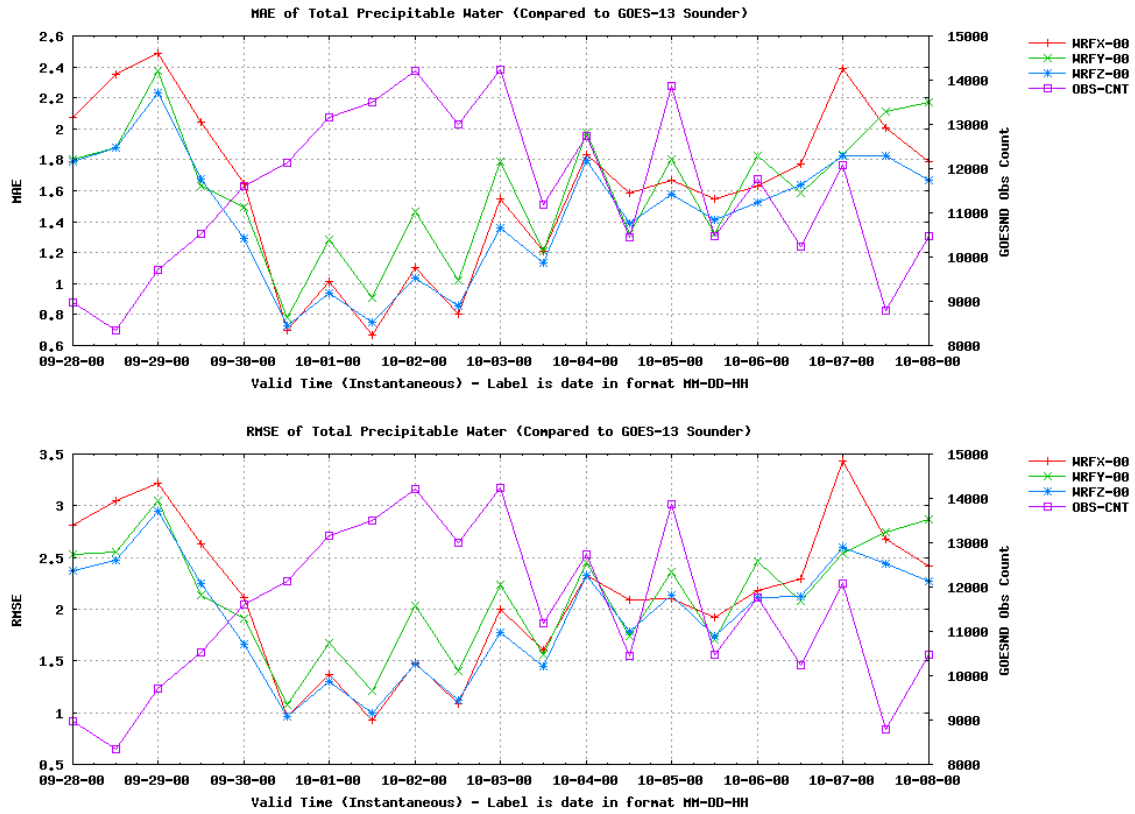


FIG. 7. Mean absolute error (top) and root-mean-square error (bottom) for total precipitable water (mm) over the period from 00 UTC 28 September 2011 to 00 UTC 8 October 2011. Error is calculated based on the GOES-13 Sounder Ma retrievals at the valid time compared to the analyses of the WRFX (red), WRFY (green), and WRFZ (blue) for the same time. The observation count (purple) is plotted on the right ordinate axis.

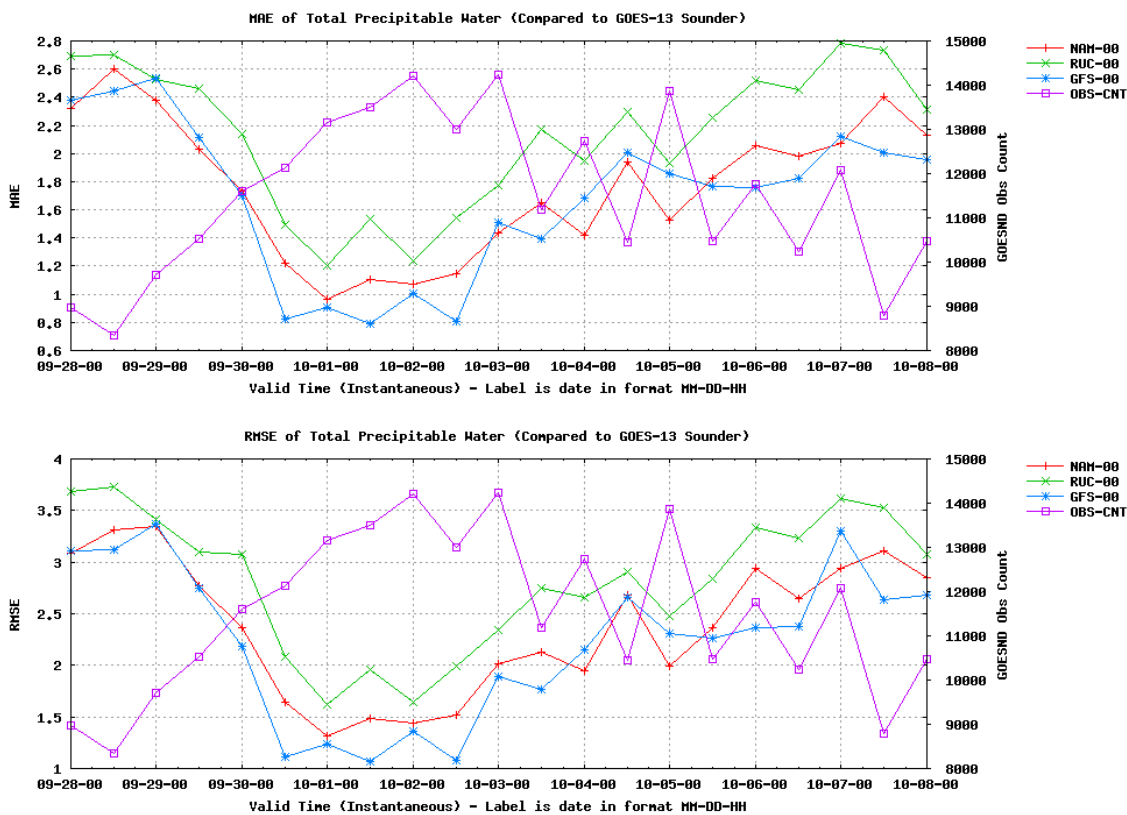


FIG. 8. Mean absolute error (top) and root-mean-square error (bottom) for total precipitable water (mm) over the period from 00 UTC 28 September 2011 to 00 UTC 8 October 2011. Error is calculated based on the GOES-13 Sounder Ma retrievals at the valid time compared to the analyses of the NAM (red), RUC (green), and GFS (blue) for the same time. The observation count (purple) is plotted on the right ordinate axis.

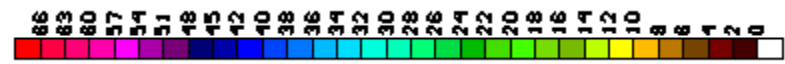
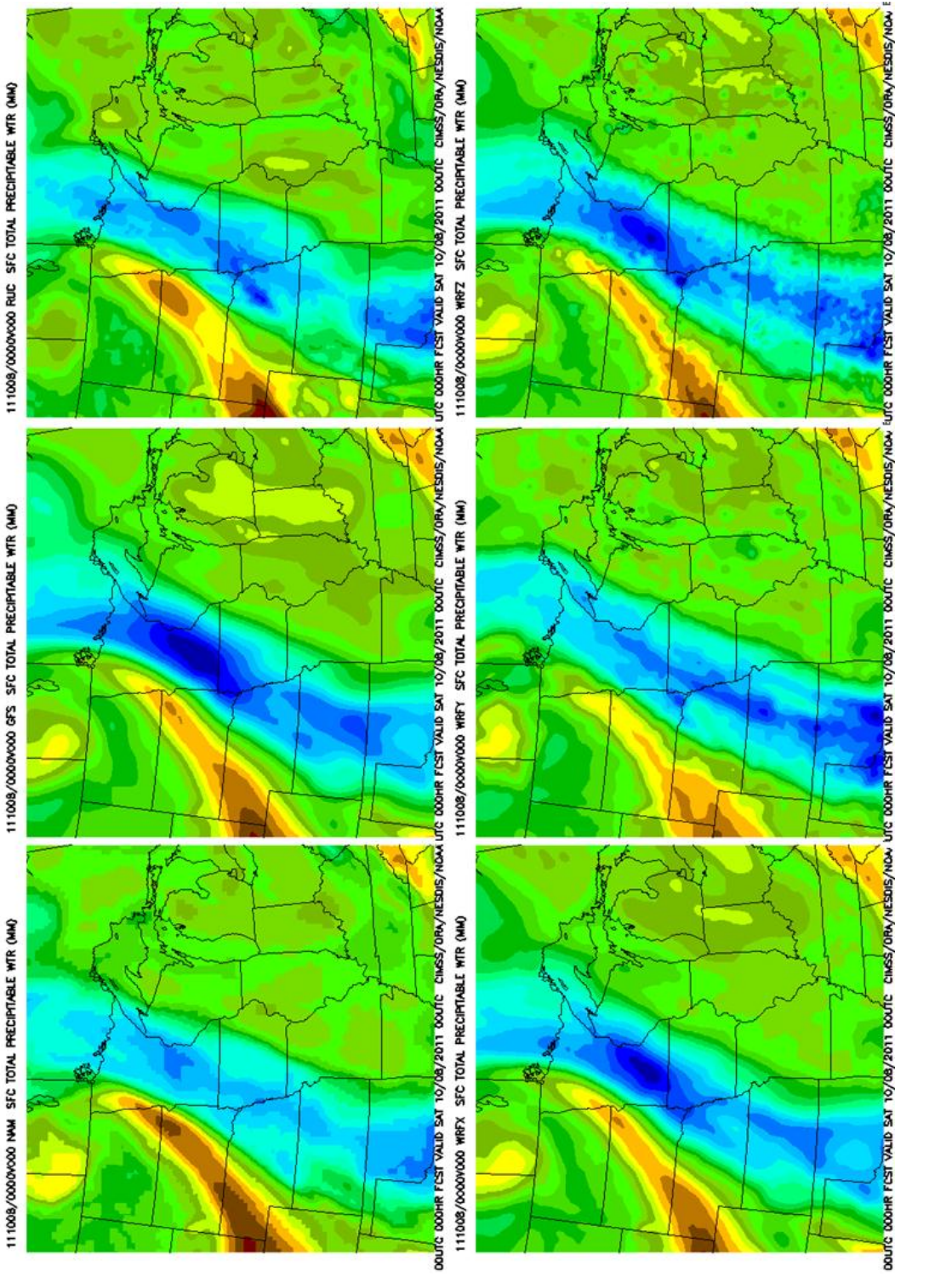


FIG. 9. The total precipitable water (mm) over the WRF model domain for subsetted analyses of the operational NCEP models (top row) and full-domain analyses of the experimental WRF simulations (bottom row) all valid at 00 UTC 8 October 2011. In order from left to right, the operational models are NAM, GFS, and RUC; the experimental models are WRFX, WRFY, and WRFZ. Blue shades indicate high precipitable water. Yellow and brown shades indicate low precipitable water.

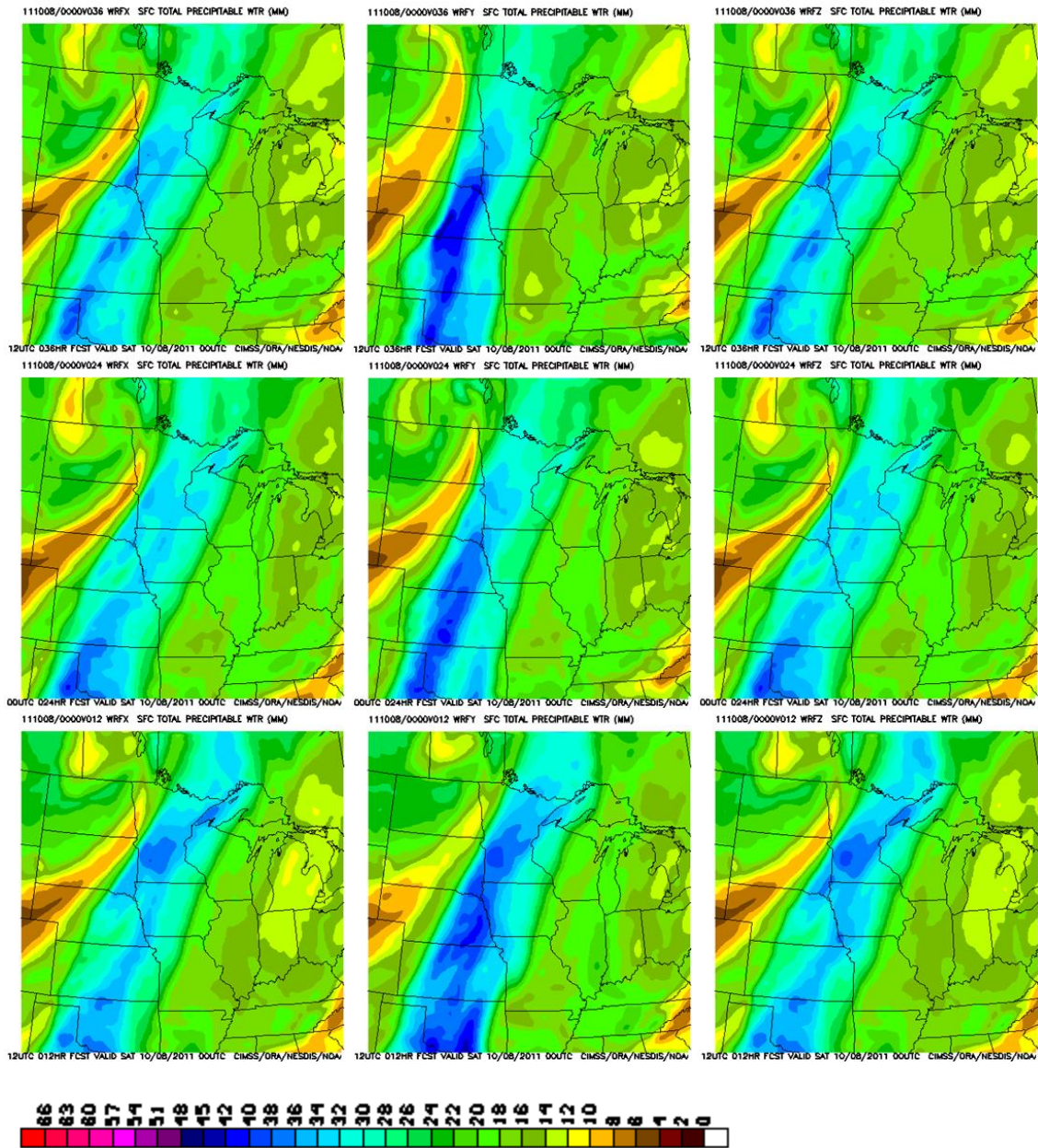


FIG. 10. The total precipitable water (mm) over the model domain for 36-hour forecasts (top row), 24-hour forecasts (middle row), and 12-hour forecasts (bottom row) from the experimental WRF simulations all valid at 00 UTC 8 October 2011. In order from left to right, the experimental models are WRFX, WRFY, and WRFZ. Blue shades indicate high precipitable water. Yellow and brown shades indicate low precipitable water.

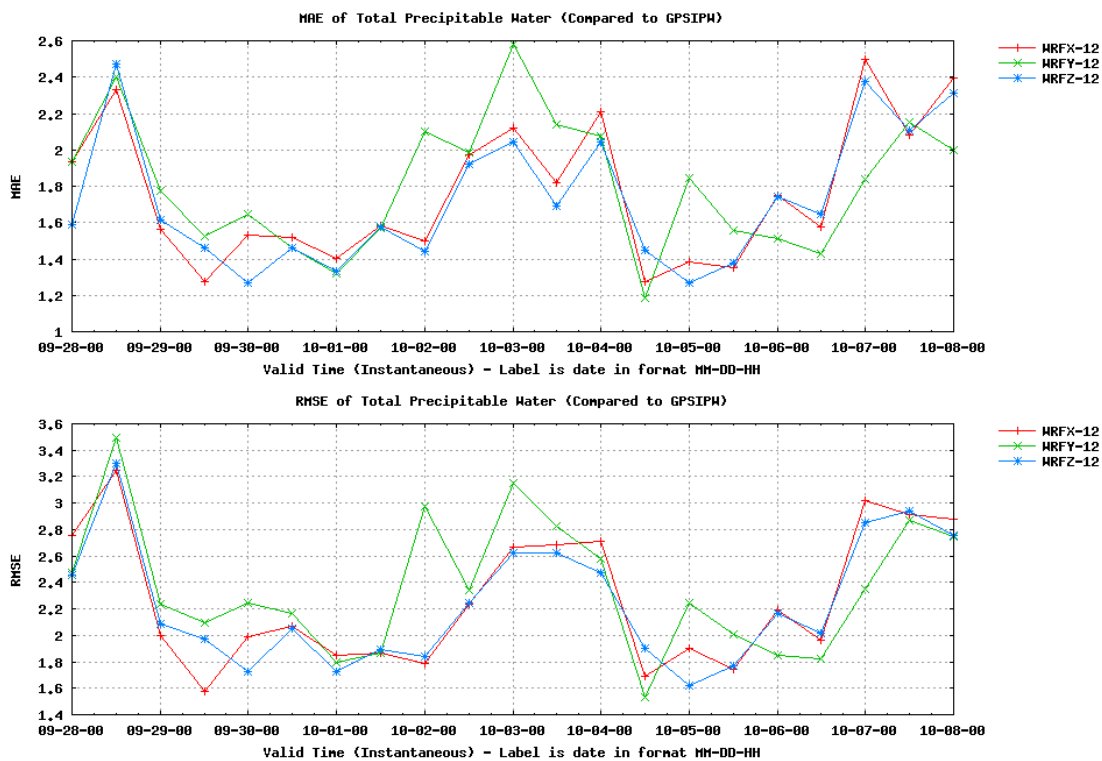


FIG. 11. Mean absolute error (top) and root-mean-square error (bottom) for total precipitable water (mm) over the period from 00 UTC 28 September 2011 to 00 UTC 8 October 2011. Error is calculated based on the GPS-IPW network at the valid time compared to the 12-hour forecasts of the WRFX (red), WRFY (green), and WRFZ (blue) for the same time.

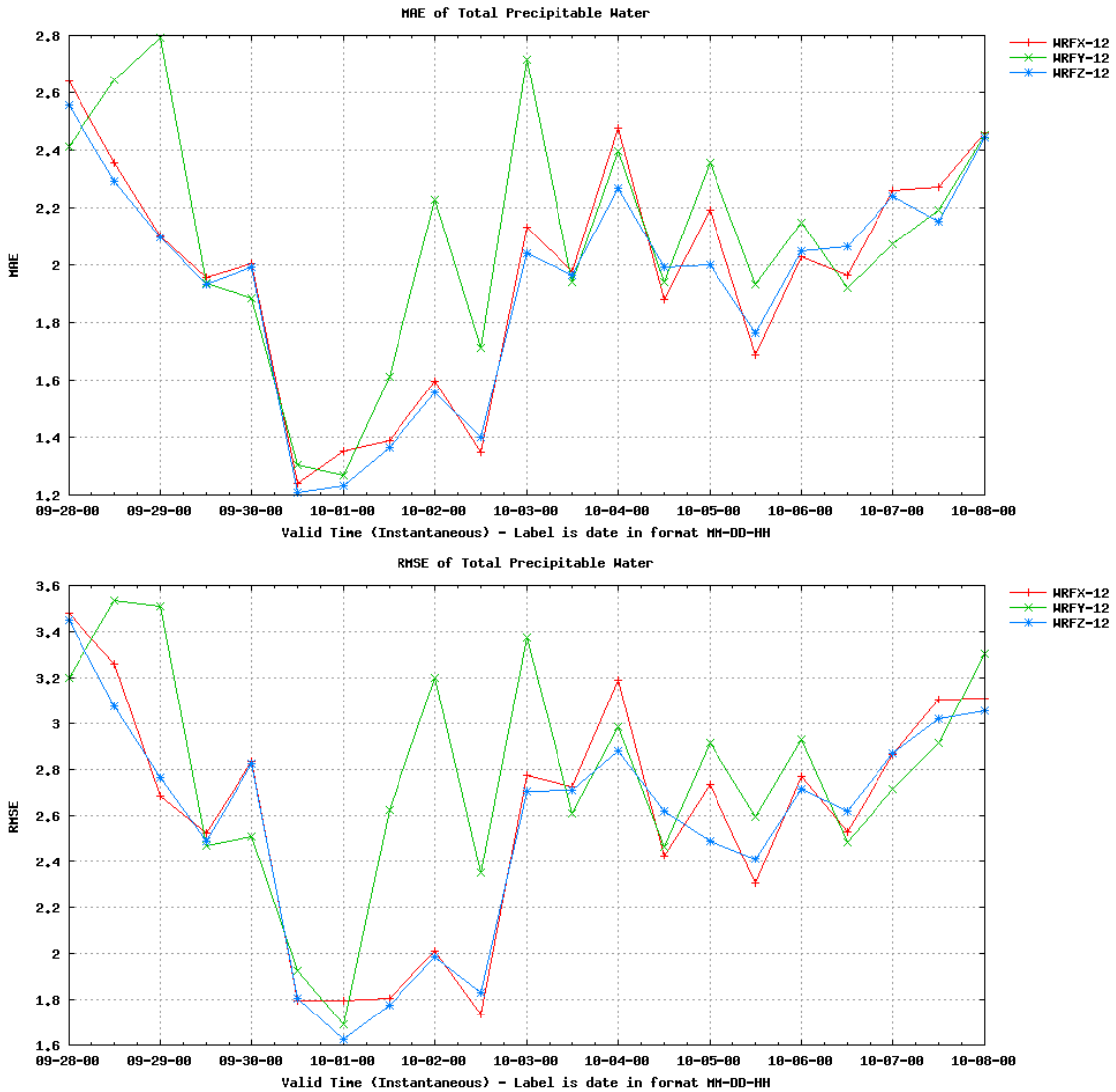


FIG. 12. Mean absolute error (top) and root-mean-square error (bottom) for total precipitable water (mm) over the period from 00 UTC 28 September 2011 to 00 UTC 8 October 2011. Error is calculated based on the NAM analysis at the valid time compared to the 12-hour forecasts of the WRFX (red), WRFY (green), and WRFZ (blue) for the same time. Note the change to the scale on the left ordinate axis between the figures.

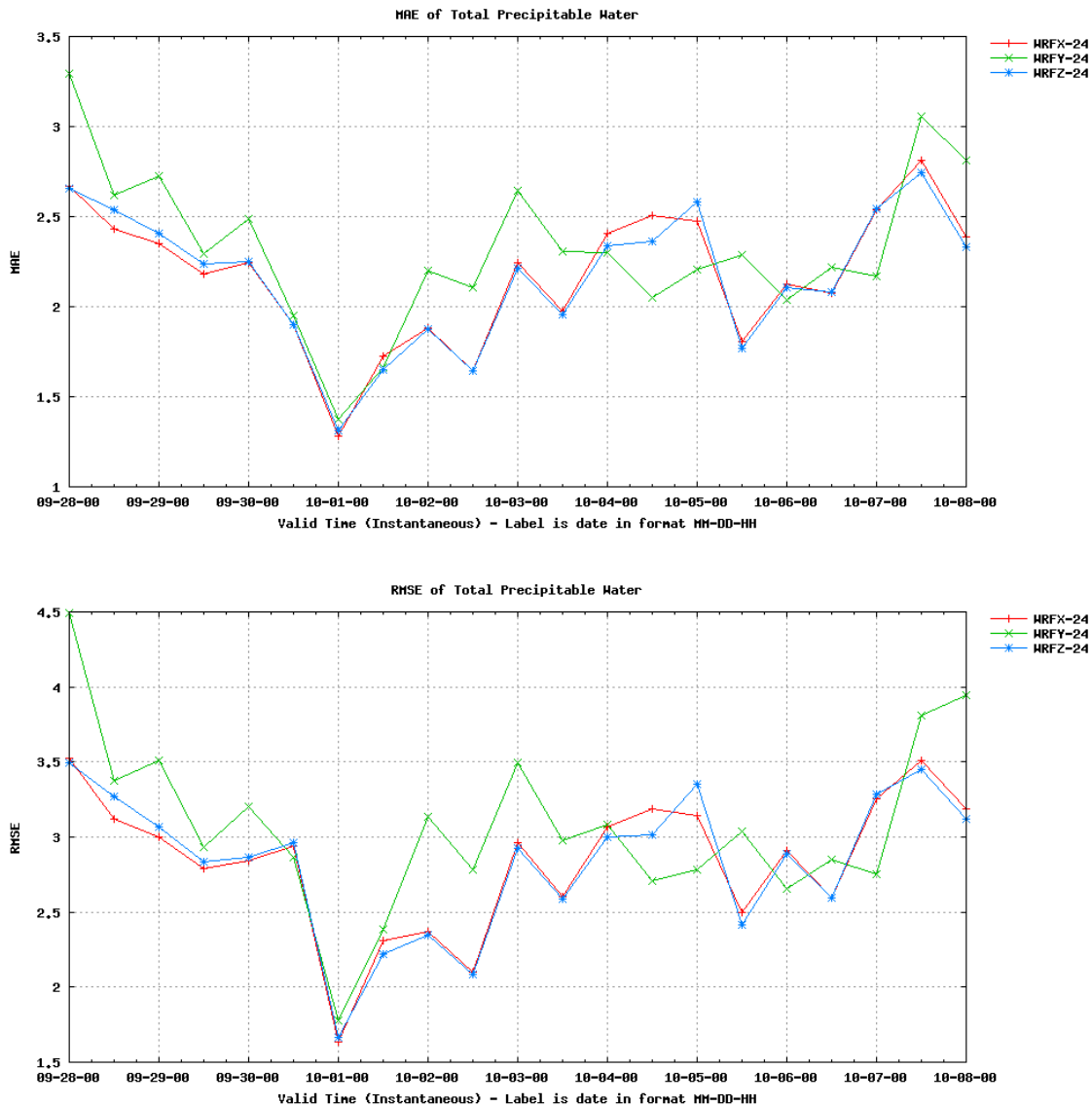


FIG. 13. Mean absolute error (top) and root-mean-square error (bottom) for total precipitable water (mm) over the period from 00 UTC 28 September 2011 to 00 UTC 8 October 2011. Error is calculated based on the NAM analysis at the valid time compared to the 24-hour forecasts of the WRFX (red), WRFY (green), and WRFZ (blue) for the same time. Note the change to the scale on the left ordinate axis between the figures.

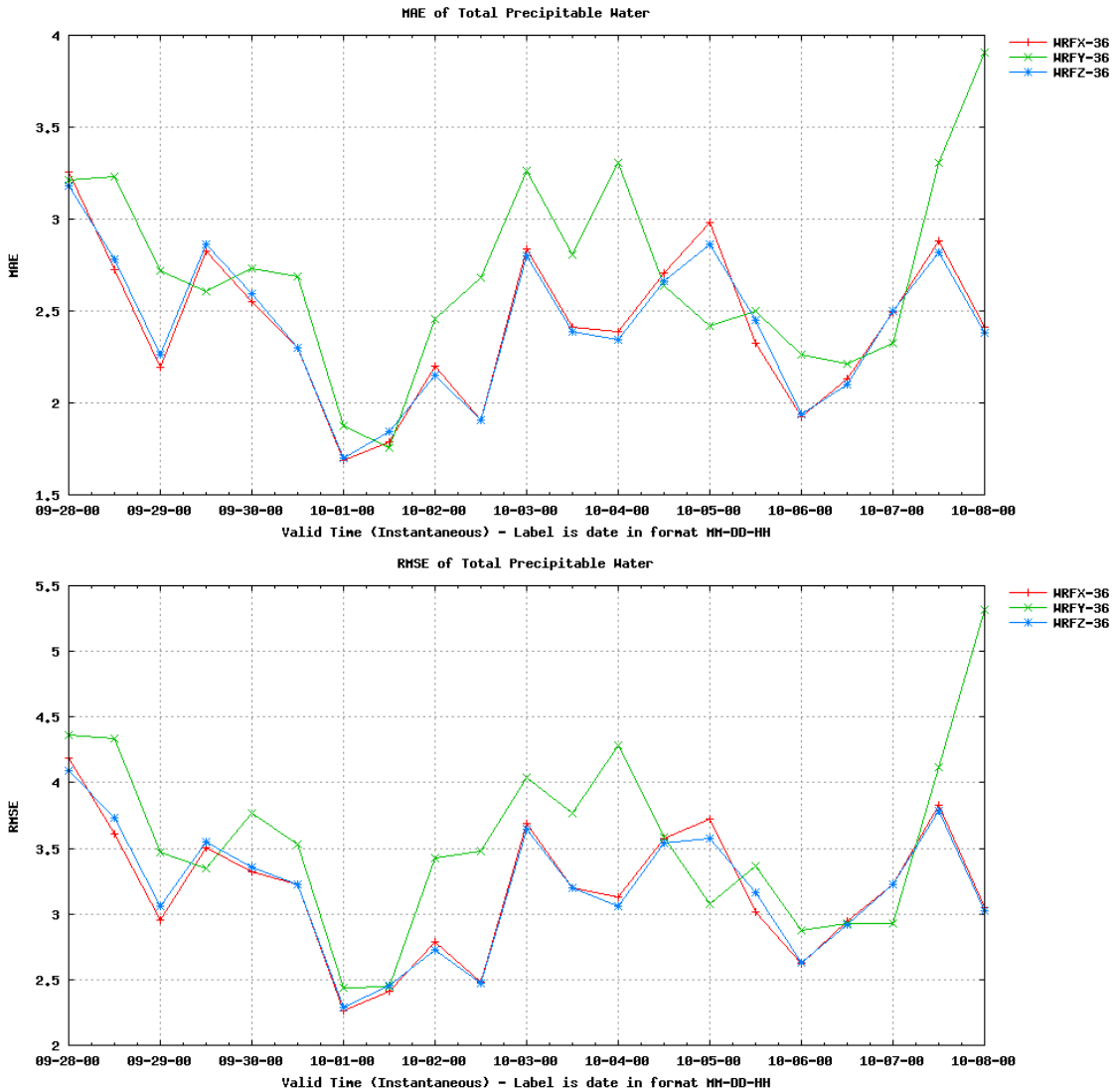


FIG. 14. Mean absolute error (top) and root-mean-square error (bottom) for total precipitable water (mm) over the period from 00 UTC 28 September 2011 to 00 UTC 8 October 2011. Error is calculated based on the NAM analysis at the valid time compared to the 36-hour forecasts of the WRFX (red), WRFY (green), and WRFZ (blue) for the same time. Note the change to the scale on the left ordinate axis between the figures.

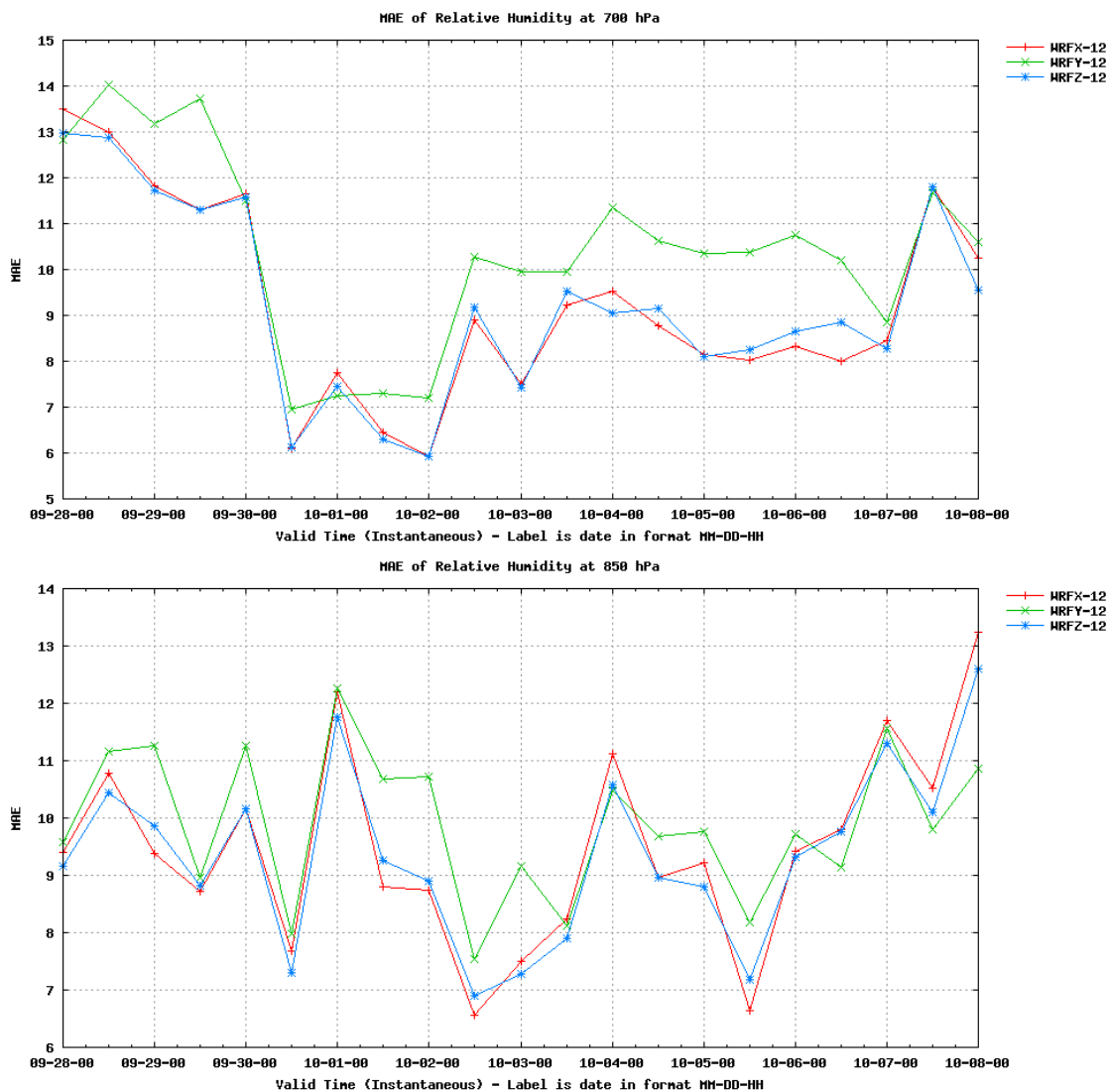


FIG. 15. Mean absolute error for relative humidity (%) at 700 hPa (top) and 850 hPa (bottom) over the period from 00 UTC 28 September 2011 to 00 UTC 8 October 2011. Error is calculated based on the NAM analysis at the valid time compared to the 12-hour forecasts of the WRFX (red), WRFY (green), and WRFZ (blue) for the same time. Note the change to the scale on the left ordinate axis between the figures.

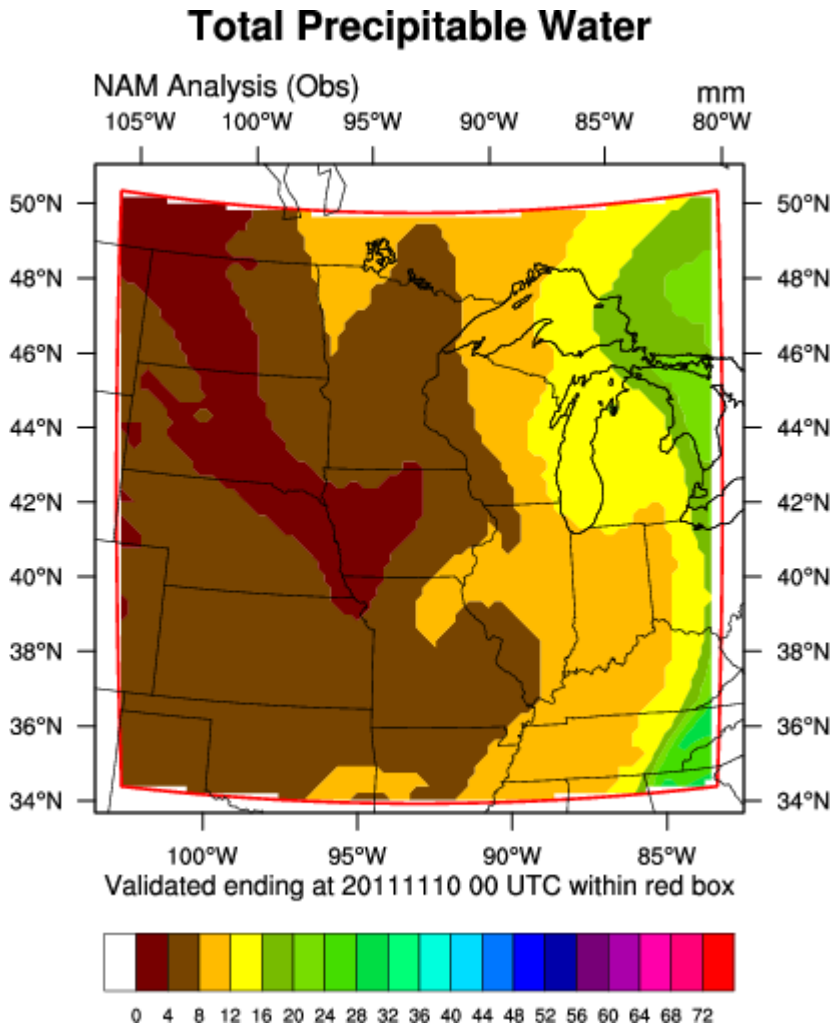


FIG. 16. The total precipitable water (mm) analysis valid at 00 UTC 10 November 2011 from the NAM. The box bounding the map is the simulation domain; the red outline is the verification domain.

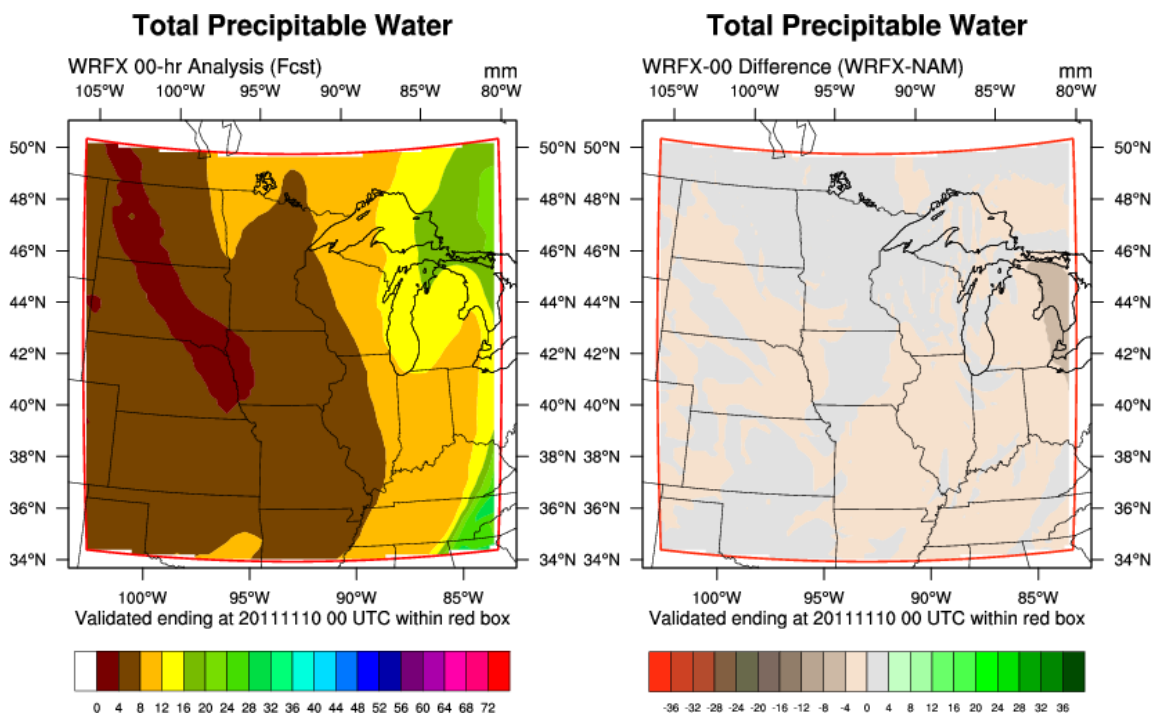


FIG. 17. The total precipitable water (mm) analysis valid at 00 UTC 10 November 2011 from the WRFX control run (left) and a difference between the WRFX and NAM analyses for the same time (right), where WRFX total precipitable water is higher in green areas and lower in brown and red areas. WRFX initial conditions are from the six-hour forecast of the previous operational GFS run. The box bounding the map is the simulation domain; the red outline is the verification domain. The WRFX MAE for this analysis, calculated from the NAM analysis, is 0.95 mm.

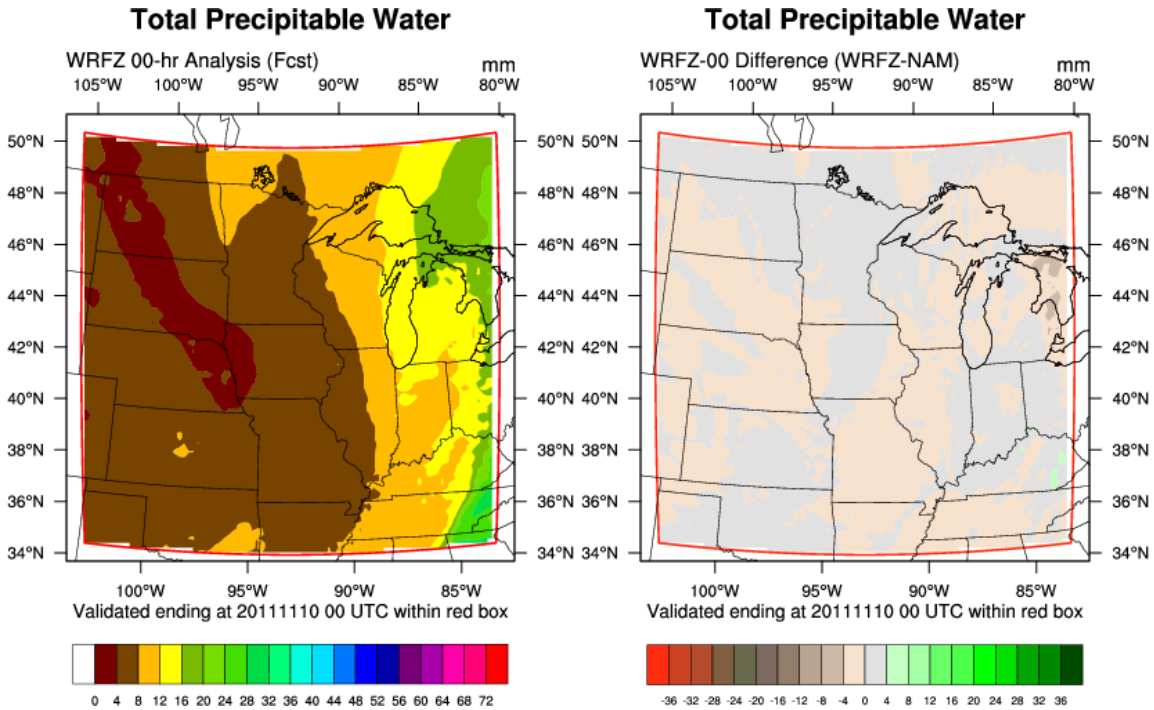


FIG. 18. The total precipitable water (mm) analysis valid at 00 UTC 10 November 2011 from the WRFZ experiment run (left) and a difference between the WRFZ and NAM analyses for the same time (right), where WRFZ total precipitable water is higher in green areas and lower in brown and red areas. WRFZ initial conditions are from the six-hour forecast of the previous operational GFS run adjusted with cloud and moisture retrievals from the GOES-13 Sounder. The box bounding the map is the simulation domain; the red outline is the verification domain. The WRFZ MAE for this analysis, calculated from the available GPS-IPW observations, is 1.07 mm.

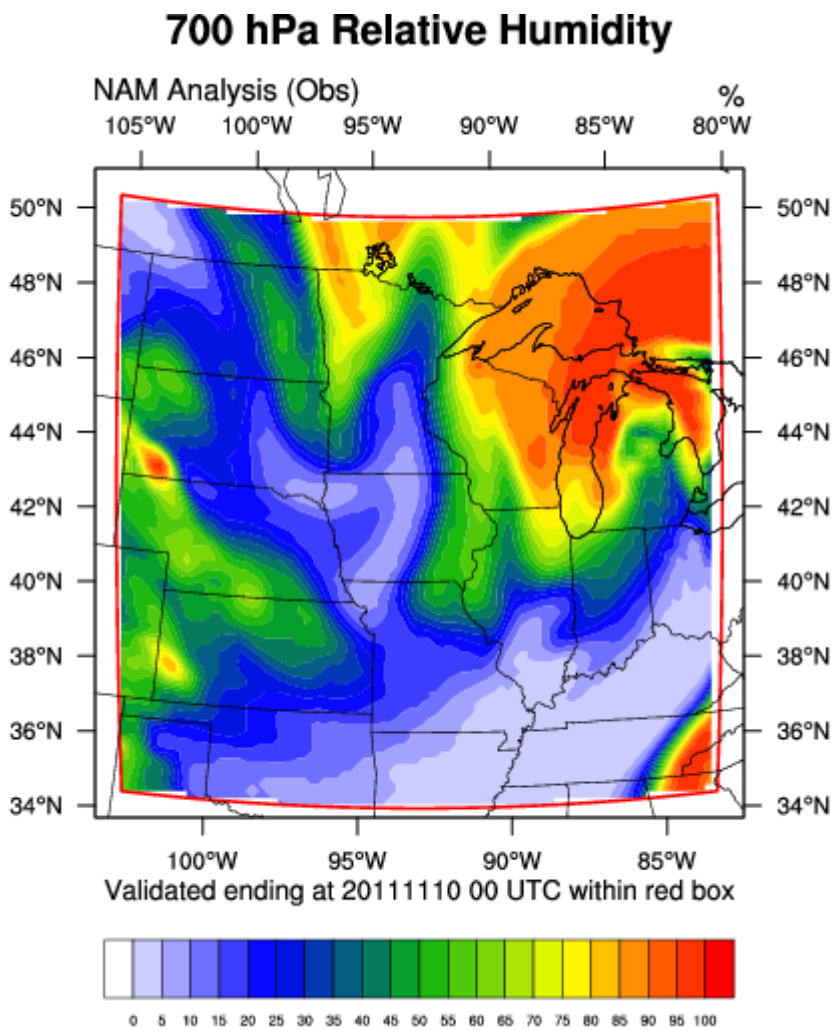


FIG. 19. The 700 hPa relative humidity (%) analysis valid at 00 UTC 10 November 2011 from the NAM. The box bounding the map is the simulation domain; the red outline is the verification domain.

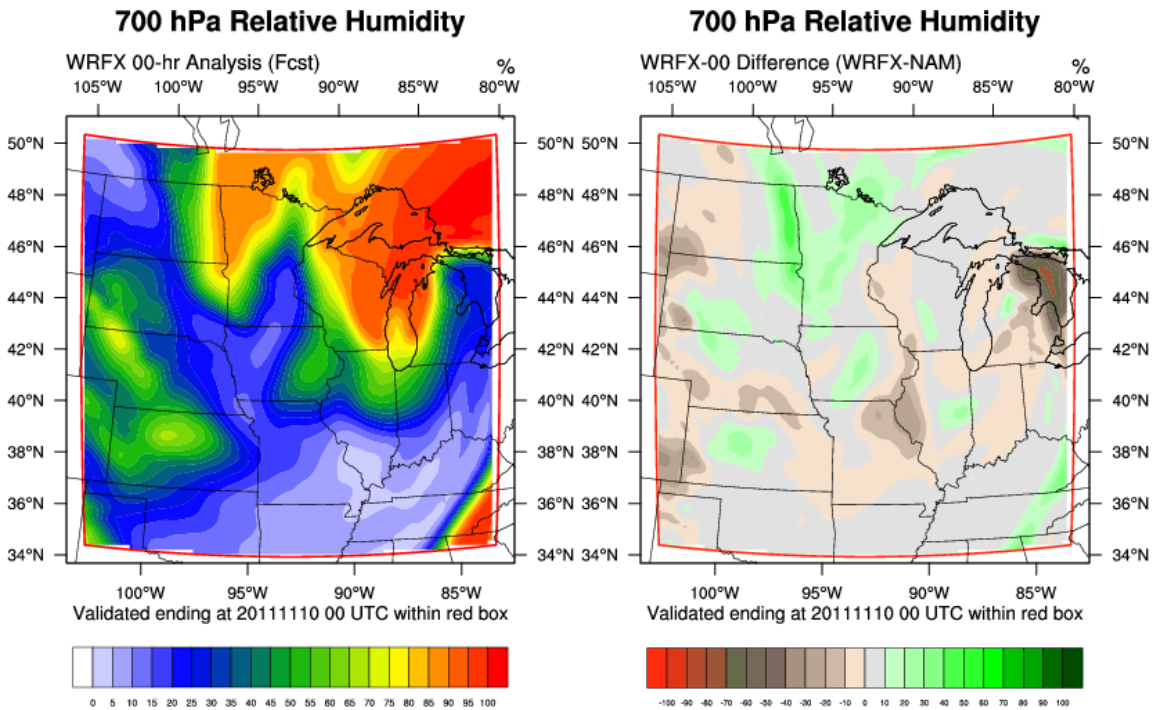


FIG. 20. The 700 hPa relative humidity (%) analysis valid at 00 UTC 10 November 2011 from the WRFX control run (left) and a difference between the WRFX and NAM analyses for the same time (right), where WRFX relative humidity is higher in green areas and lower in brown and red areas. WRFX initial conditions are from the six-hour forecast of the previous operational GFS run. The box bounding the map is the simulation domain; the red outline is the verification domain.

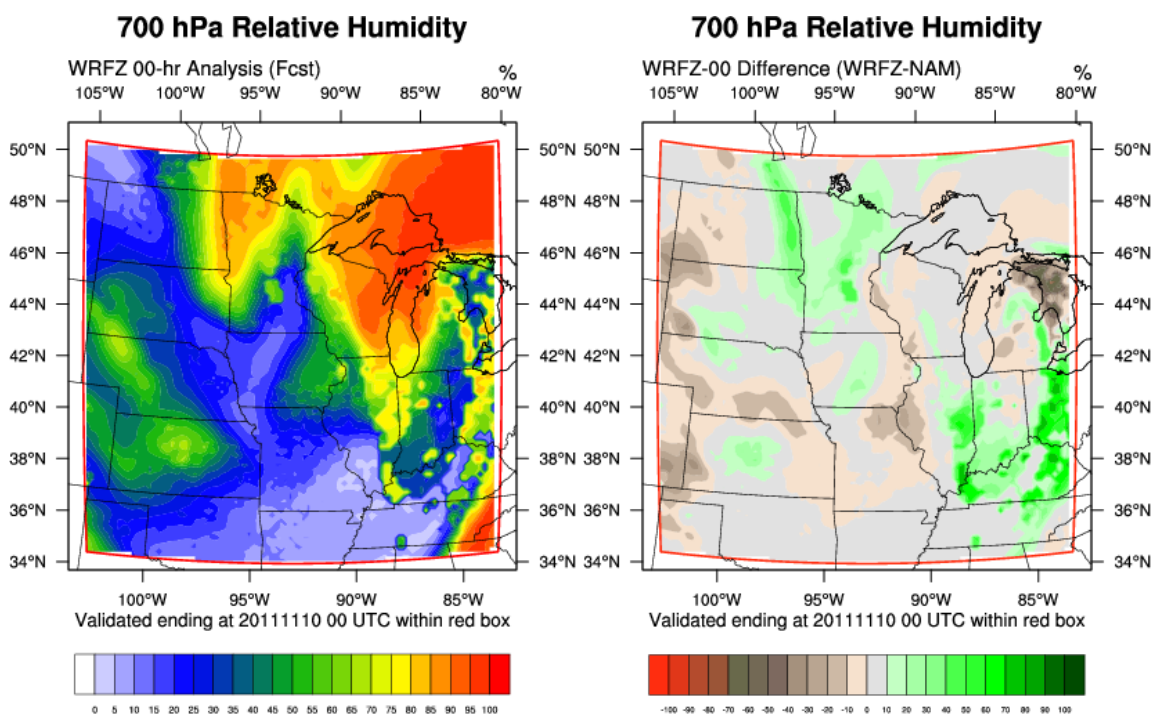


FIG. 21. The 700 hPa relative humidity analysis (%) valid at 00 UTC 10 November 2011 from the WRFZ experiment run (left) and a difference between the WRFZ and NAM analyses for the same time (right), where WRFZ relative humidity is higher in green areas and lower in brown and red areas. Local maxima in relative humidity over the Ohio Valley indicate cloudiness. WRFZ initial conditions are from the six-hour forecast of the previous operational GFS run adjusted with cloud and moisture retrievals from the GOES-13 Sounder. The box bounding the map is the simulation domain; the red outline is the verification domain.

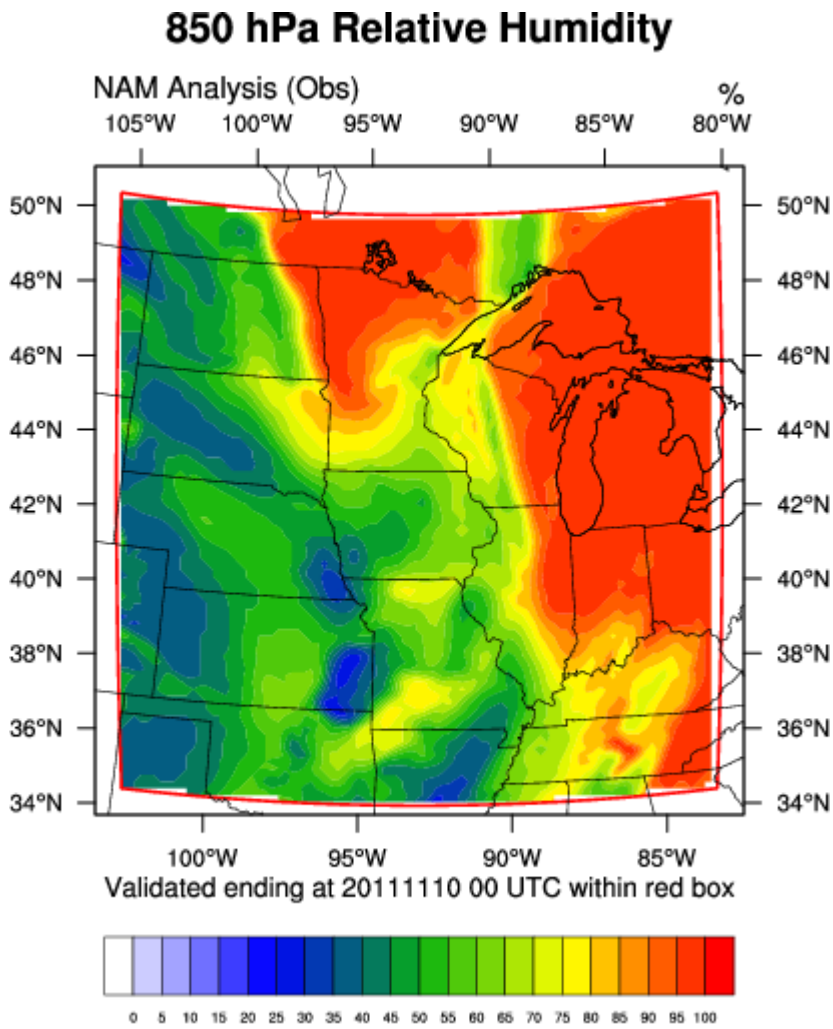


FIG. 22. The 850 hPa relative humidity (%) analysis valid at 00 UTC 10 November 2011 from the NAM. The box bounding the map is the simulation domain; the red outline is the verification domain.

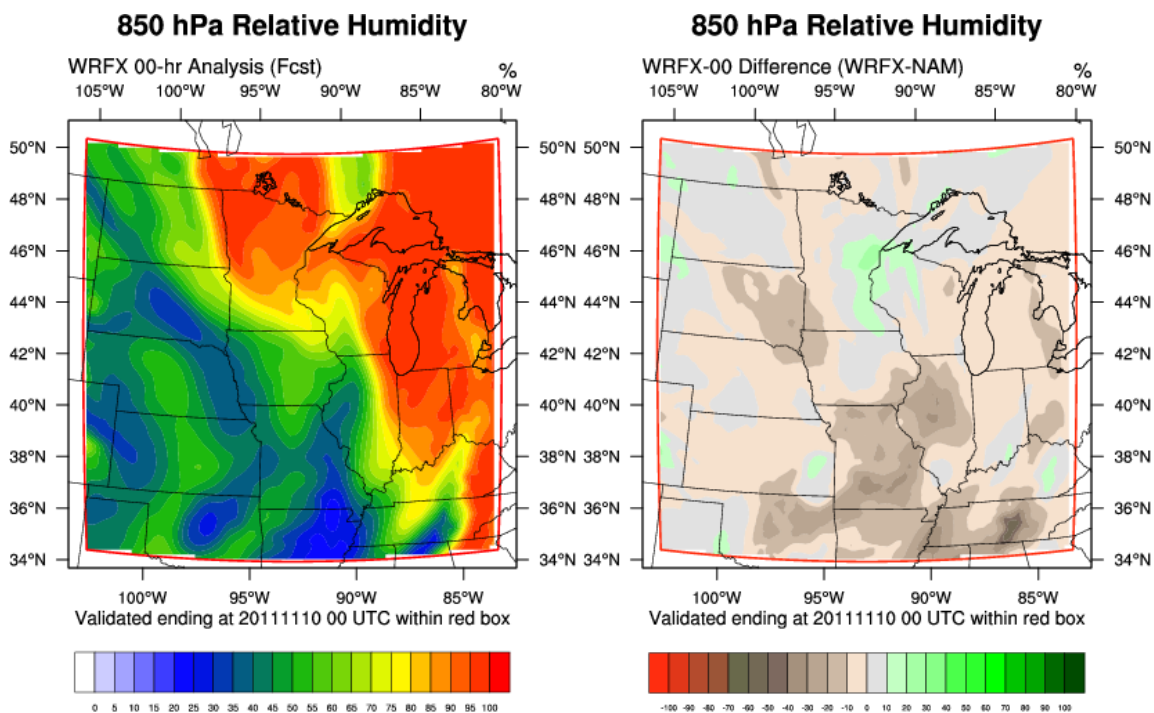


FIG. 23. The 850 hPa relative humidity (%) analysis valid at 00 UTC 10 November 2011 from the WRFX control run (left) and a difference between the WRFX and NAM analyses for the same time (right), where WRFX relative humidity is higher in green areas and lower in brown and red areas. WRFX initial conditions are from the six-hour forecast of the previous operational GFS run. The box bounding the map is the simulation domain; the red outline is the verification domain.

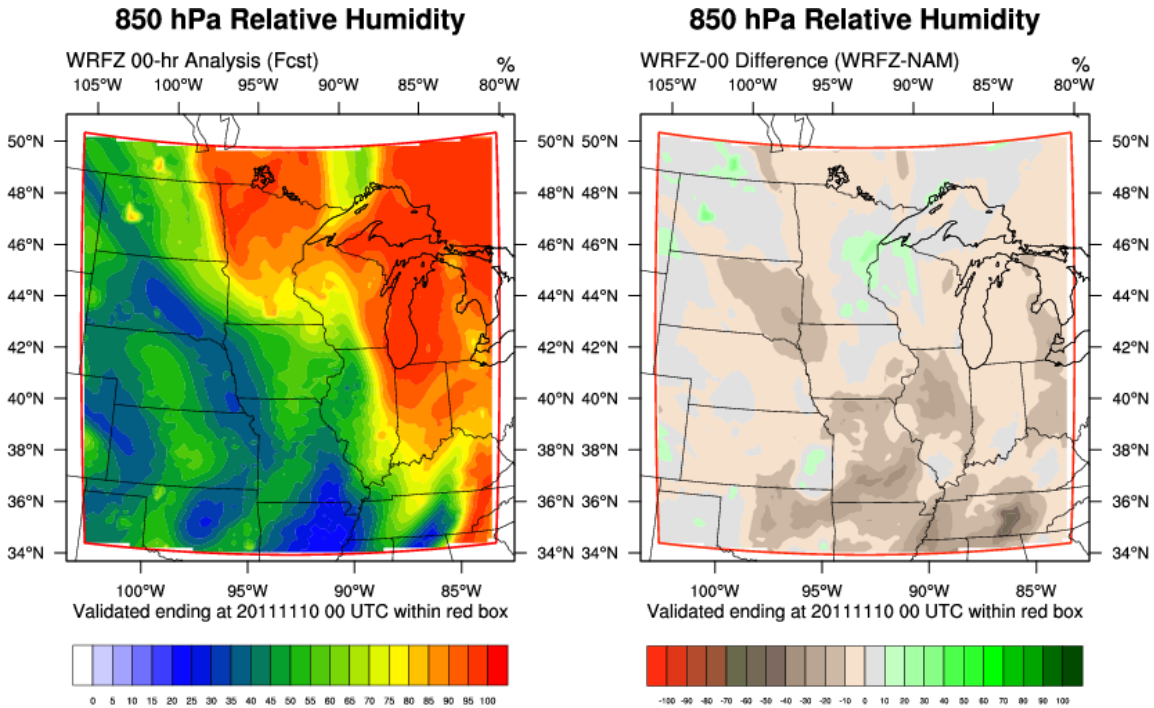


FIG. 24. The 850 hPa relative humidity (%) analysis from the WRFZ experiment run valid at 00 UTC 10 November 2011 (left) and a difference between the WRFZ and NAM analyses for the same time (right), where WRFZ relative humidity is higher in green areas and lower in brown and red areas. WRFZ initial conditions are from the six-hour forecast of the previous operational GFS run adjusted with cloud and moisture retrievals from the GOES-13 Sounder. The box bounding the map is the simulation domain; the red outline is the verification domain.

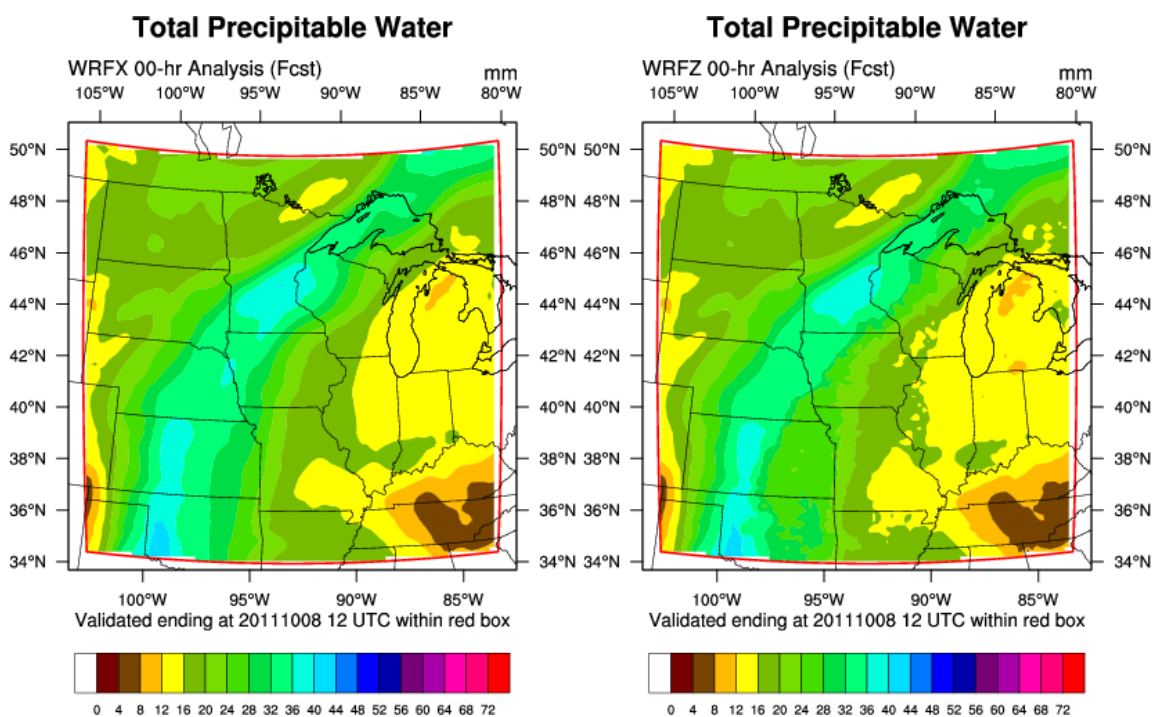
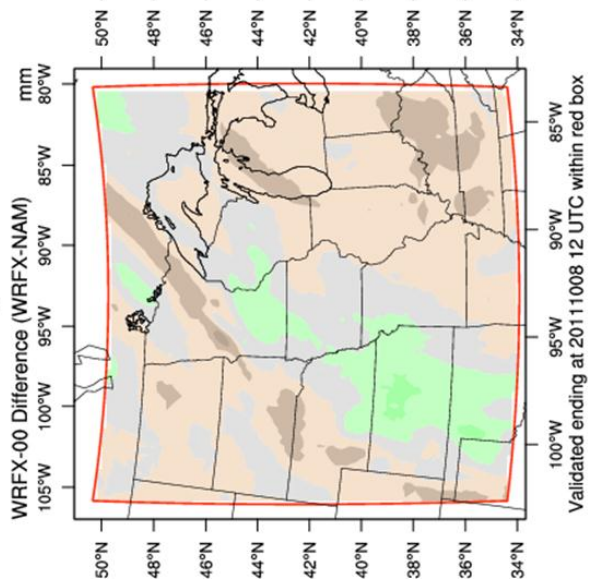
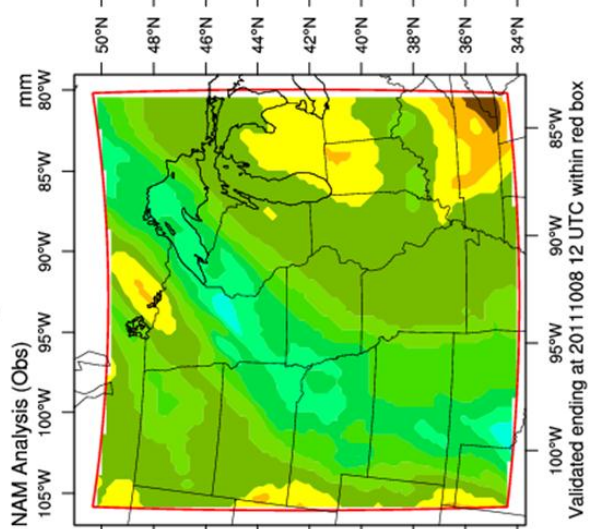


FIG. 25. The total precipitable water (mm) analyses valid at 12 UTC 8 October 2011 from the WRFX (left) and WRFZ (right). WRFZ initial conditions are from the six-hour forecast of the previous operational GFS run adjusted with cloud and moisture retrievals from the GOES-13 Sounder. WRFX does not contain Sounder input. The box bounding the map is the simulation domain; the red outline is the verification domain.

Total Precipitable Water



Total Precipitable Water



Total Precipitable Water

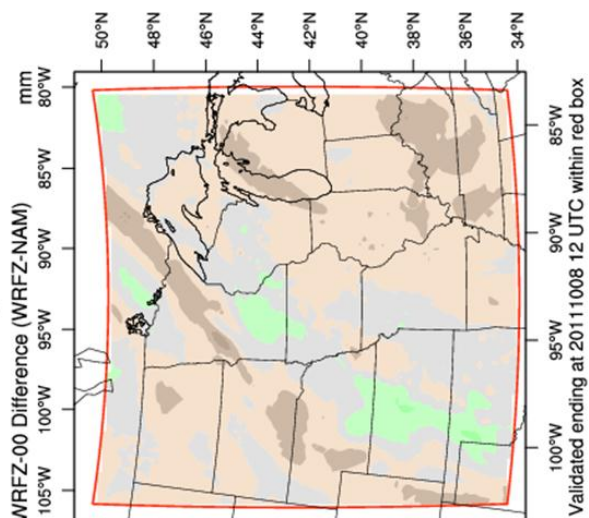
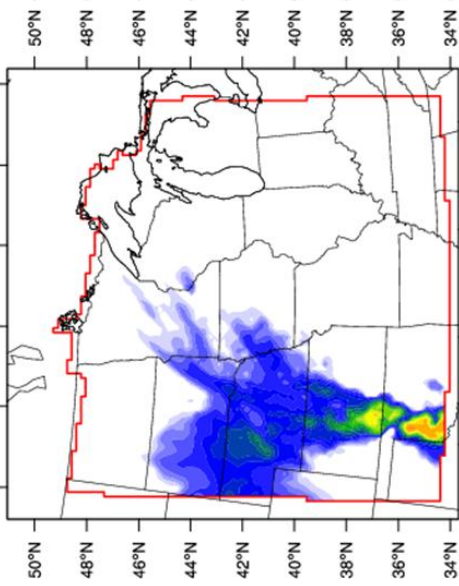


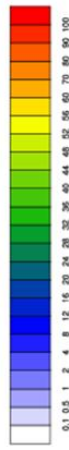
FIG. 26. The total precipitable water (mm) analysis valid at 12 UTC 8 October 2011 from the NAM (center), a difference between the WRFX and NAM analyses (left), and a difference between the WRFZ and NAM analyses (right). For the difference plots, NAM total precipitable water is higher than the WRF run in brown and red areas and lower in the green areas. WRFZ initial conditions are from the six-hour forecast of the previous operational GFS run adjusted with cloud and moisture retrievals from the GOES-13 Sounder. WRFX does not contain Sounder input. The box bounding the map is the simulation domain; the red outline is the verification domain. The WRFZ (right) MAE computed based on the GPS-IPW observations is 1.58 mm, compared to 1.87 mm from the WRFX (left).

12-hr Accumulated Precipitation

WRFX-12 Forecast (Fcst) mm
105°W 100°W 95°W 90°W 85°W 80°W

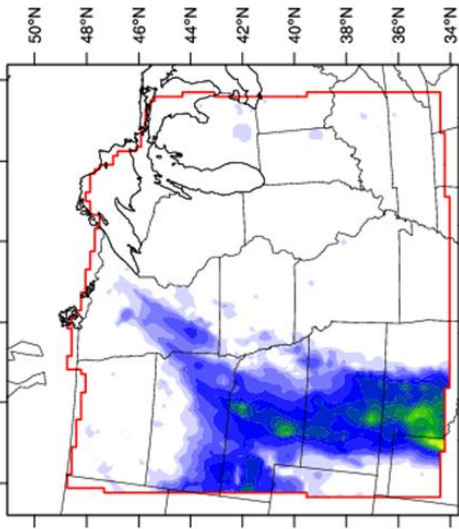


Validated ending at 20111009 00 UTC within red box

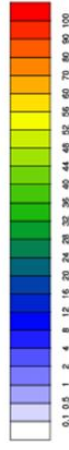


12-hr Accumulated Precipitation

Stage II Observation (Obs) mm
105°W 100°W 95°W 90°W 85°W 80°W

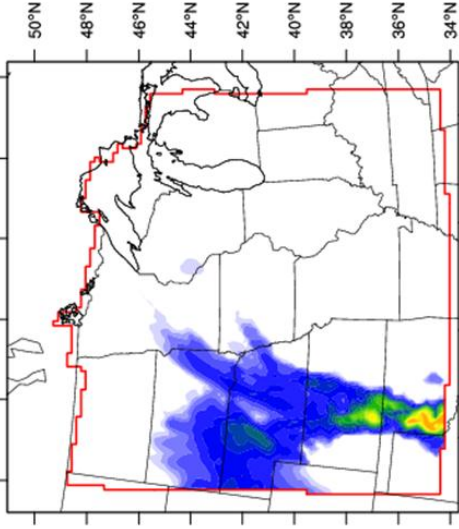


Validated ending at 20111009 00 UTC within red box



12-hr Accumulated Precipitation

WRFZ-12 Forecast (Fcst) mm
105°W 100°W 95°W 90°W 85°W 80°W



Validated ending at 20111009 00 UTC within red box

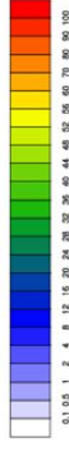


FIG. 27. The 12-hour accumulated precipitation (mm) valid ending at 00 UTC 9 October 2011 from the NCEP Stage II multi-sensor analysis (center), WRFX 12-hour forecast (left), and WRFZ 12-hour forecast (right). WRFZ initial conditions are from the six-hour forecast of the previous operational GFS run adjusted with cloud and moisture retrievals from the GOES-13 Sounder. WRFX does not contain Sounder input. The box bounding the map is the simulation domain; the red outline is the verification domain. The WRFZ (right) MAE computed based on the Stage II analysis is 1.48 mm, compared to 1.65 mm from the WRFX (left).

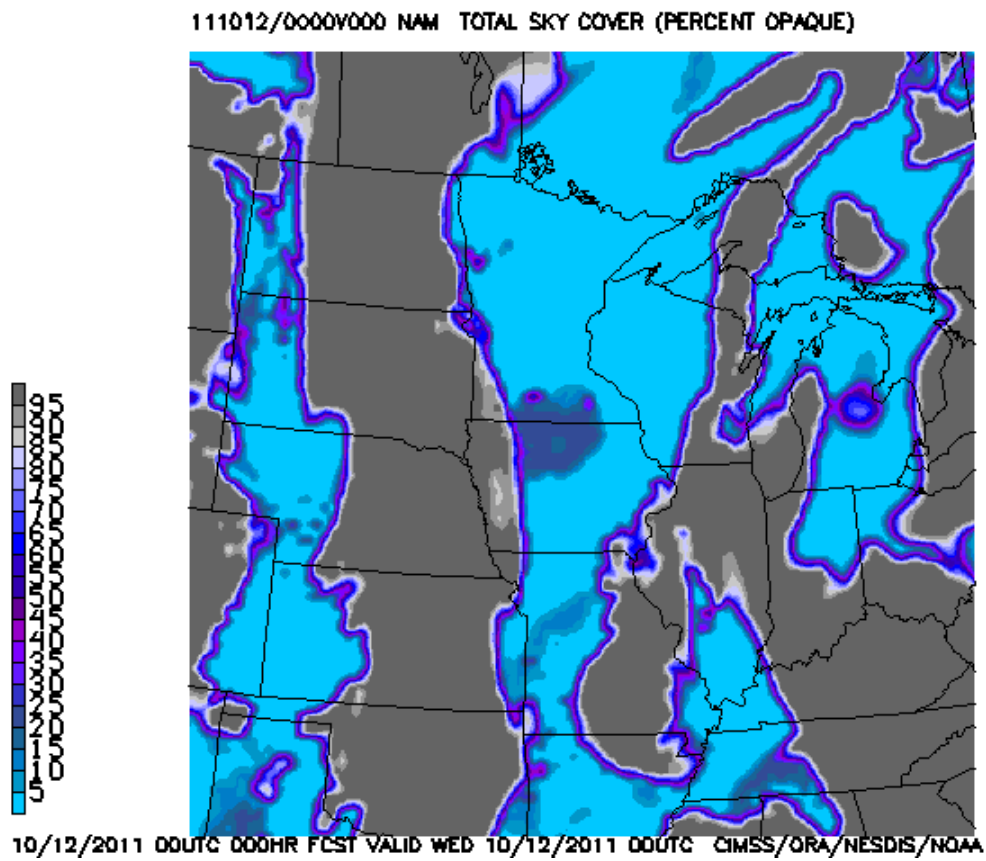


FIG. 28. The NAM analysis of total sky cover (%) valid at 00 UTC 12 October 2011.

Cyan areas indicate clear sky; grey areas represent overcast.

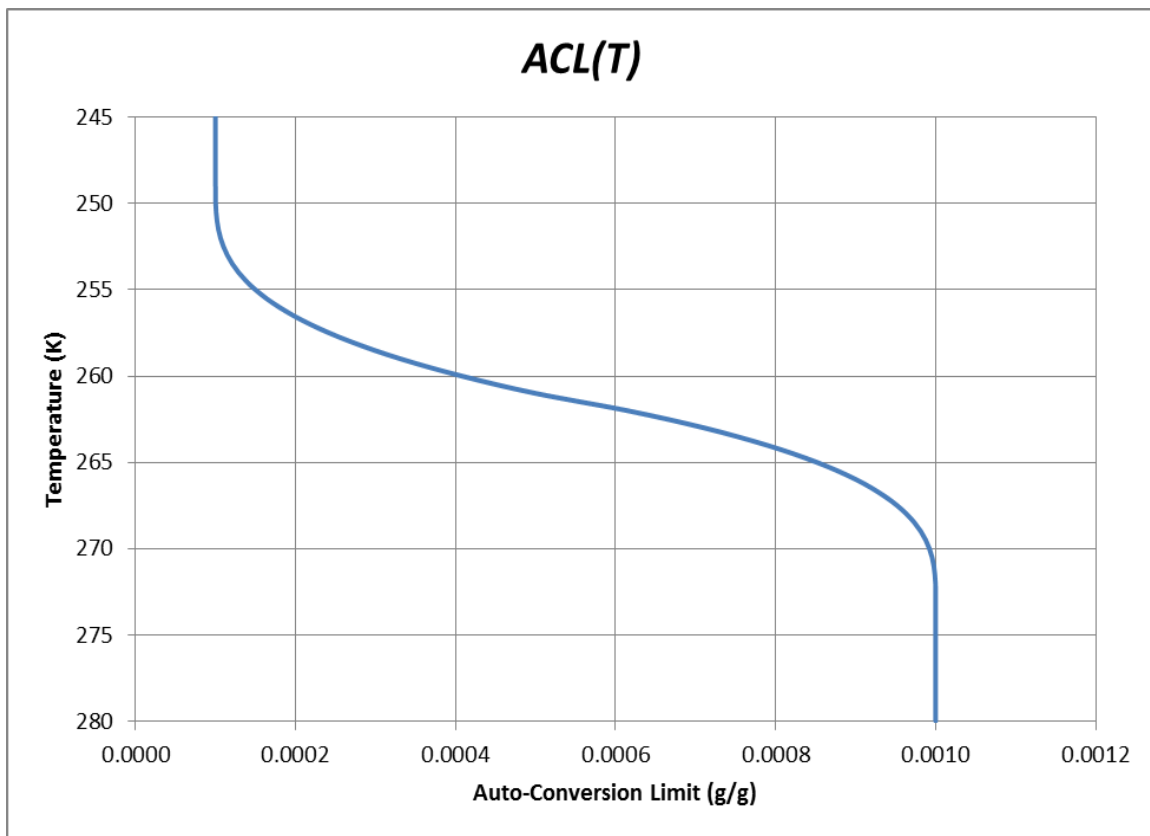


FIG. 29. The cloud-to-precipitation auto-conversion limit (ACL) as a function of temperature (T) that is used in the CRAS. The ACL is used to calculate the cloud fraction.

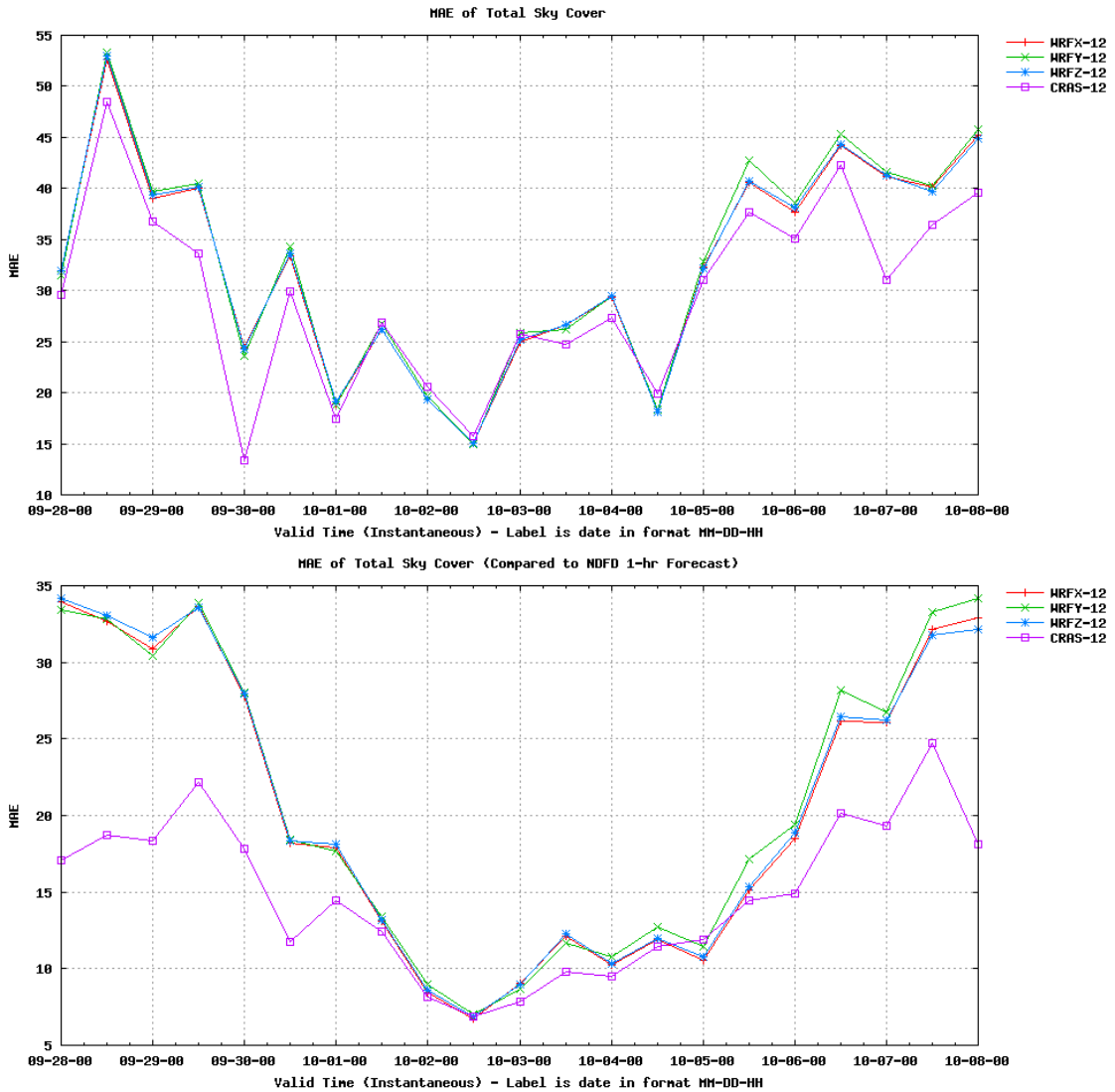


FIG. 30. Mean absolute error for total sky cover (%) over the period from 00 UTC 28 September 2011 to 00 UTC 8 October 2011. Error is calculated based on the NAM analysis (top) and NDFD 1-hour forecast (bottom) at the valid time compared to the 12-hour forecasts of the WRFX (red), WRFY (green), WRFZ (blue), and CRAS (purple) for the same time. The WRF sky cover was calculated using the default algorithm. Note the change to the scale on the left ordinate axis between the figures.

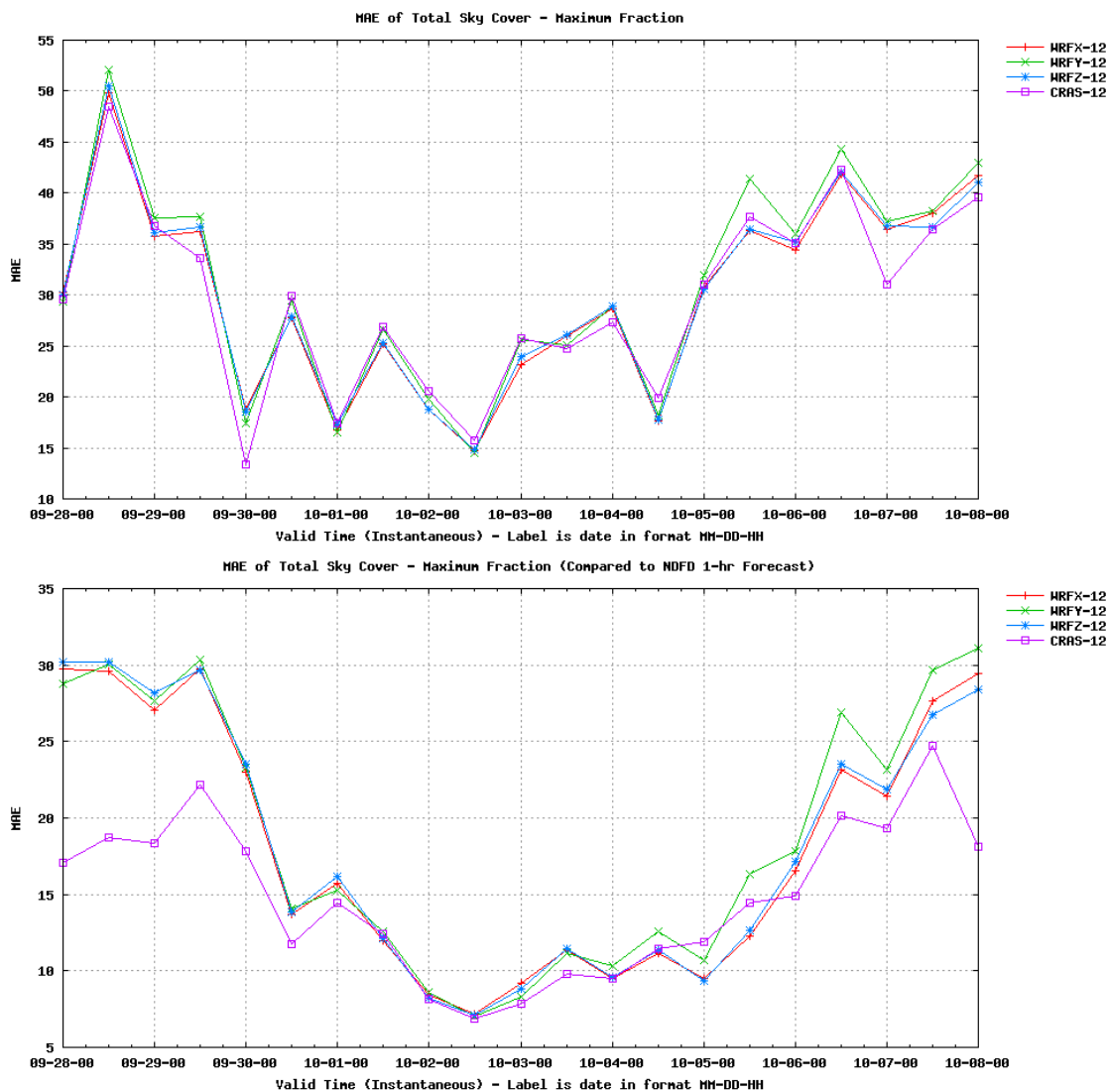


FIG. 31. Mean absolute error for total sky cover (%) over the period from 00 UTC 28 September 2011 to 00 UTC 8 October 2011. Error is calculated based on the NAM analysis (top) and NDFD 1-hour forecast (bottom) at the valid time compared to the 12-hour forecasts of the WRFX (red), WRFY (green), WRFZ (blue), and CRAS (purple) for the same time. The WRF sky cover was calculated using the layer with the highest fraction for each grid point. Note the change to the scale on the left ordinate axis between the figures.

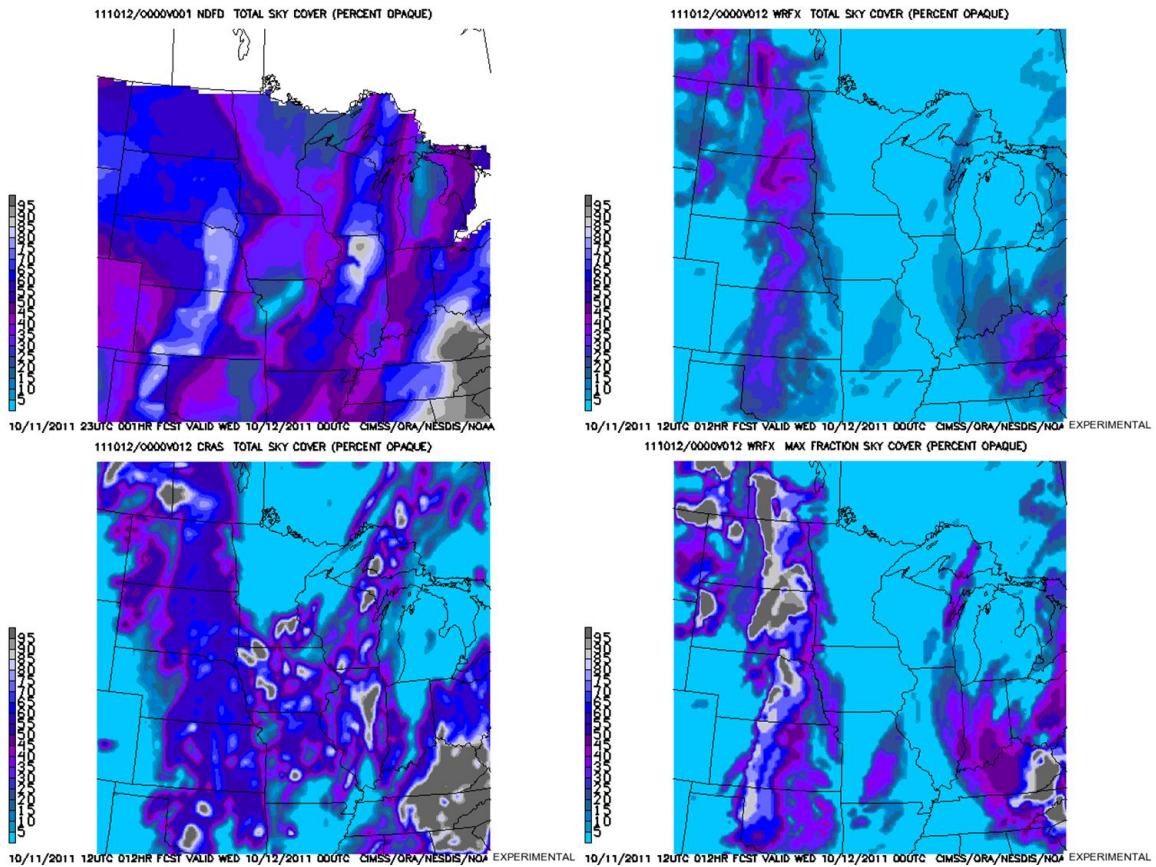


FIG. 32. The NDFD one-hour total sky cover forecast (upper left), CRAS 12-hour forecast of total sky cover (lower left), WRFX 12-hour forecast of total sky cover using the default calculation (upper right), and WRFX 12-hour forecast of total sky cover using the maximum-layer calculation (lower right) all valid at 00 UTC 12 October 2011. The WRFY and WRFZ forecasts are not shown due to their similarity to the WRFX. Cyan areas indicate clear sky; grey areas represent overcast. Units are percent covered for all plots.